Photo-induced ionization of the nitrogen-vacancy center

Loutfi Kuret

Master of Science

Physics Department

McGill University

Montreal,Quebec

August 2015

A thesis submitted to McGill University in partial fulfillment of the requirements of the degree of Master of Science

ACKNOWLEDGEMENTS

I would like to thank my supervisor Pr. Lilian Childress for her numerous guidance and for being so considerate when motivation was low.

I would also like to thank Zackary Flansberry whose contribution to the design and construction of the confocal microscope is very appreciated.

Also, special thanks to Benjamin D'Anjou for his help in providing the theoretical tools for extracting the ionization rates and the charge state measurement fidelity.

ABSTRACT

The nitrogen-vacancy (NV) center has emerged, in solid state physics, as a very strong candidate for quantum computation as well as for metrology applications. Although very promising, NV center systems remain very hard to control due to their large number of quantum states. This thesis presents work to understand one aspect of the NV center many degrees of freedom : the ionization process of the nitrogen-vacancy center. To accomplish this goal, a confocal microscope for the study and detection of defects was built. For the control of experimental sequences, an arbitrary Pulse-Pattern Generator using a Field Programmable Gate Array (FPGA) card in a LabView environment was developed. Finally, the switching rates associated with blinking induced by ionization of the NV center were measured and a fidelity measurement for the charge state (NV^- and NV^0) detection of the NV center was performed.

ABRÉGÉ

Ce projet de thèse de maîtrise est composée de trois sections différentes. La premiòre partie consiste à décrire la construction d'un microscope confocal pour l'étude et la détection de défauts dans les diamants appelé centre NV. Pour le controle de séquences expérimentales, la deuxième partie détaille le développement d'un générateur d'impulsion arbitraire en utilisant une carte FPGA dans un environnement LabVIEW. La section finale consiste à mesurer les taux de saut (Γ_- and Γ_+) associés aux clignotement induite par ionisation du centre NV ainsi que l'obtention d'une mesure de la fidélité pour la détection de l'état de charge (NV^- and NV^0) du centre NV.

TABLE OF CONTENTS

LIST OF TABLES

LIST OF FIGURES

CHAPTER 1
Introduction

In the early 1980s, nobel laureate Richard Feynman among others, raised the question can quantum systems can be probabilistically simulated by a classical computer [1]. Since the answer to this question is believed to be no, the idea of generalizing information science to quantum processes to properly simulate any physical system started gaining popularity. In 1985, David Deutsch mathematically described a universal quantum computer capable of simulating every finite, realizable physical system [2]. Later in 1994, Peter W. Shor developed an algorithm using quantum operations for factoring numbers much faster than a conventional computer [3]. Shor's algorithm led to a worldwide interest in building a physical quantum computer. Potential candidates for quantum computation span a large array of physical systems, for example quantum bits (qubits) using single photons [4], trapped atoms [5], quantum dots [6], superconducting circuits [7] and many others. For the sake of this thesis, we will concentrate on spin based quantum systems.

1.1 Spin-based quantum computing

In solid-state structures, spin-based systems are especially interesting due to their simple and well isolated quantum system, their long decoherence times, and easy to implement gate operations. A spin-based quantum computer makes use of the nuclear spin or electronic spin of an atom or molecule to form a qubit. Nuclear spins are especially interesting because of their extremely good

isolation from electronic and vibrational mechanisms that can lead to decoherence. On the other hand, electronic spins are much more sensitive to their environment which leads to much easier initialization, manipulation, and read out mechanisms. However, because of their sensitivity, electronic spins have shorter coherence times compared to nuclear spins. Many existing systems use either the nuclear spin or electronic spin as qubit. For example, one of the earliest realizations used bulk nuclear spin-resonance of molecules to create a 2 qubit NMR quantum computer [8]. Other systems, such as GaAs quantum dots [9] and Fullerene-based systems [10] have been successful for utilizing the electronic spin state for quantum computation purposes.

1.2 Nitrogen-vacancy Center

One appealing idea is to develop a hybrid system consisting of qubits of different species each optimized for its specific task. One approach to these kind of quantum processors is based on nodes of nuclear spins to store information and that are locally controlled via an individually addressable electron spin used to couple qubits together. One of these hybrid candidates is called the nitrogen-vacancy (NV) center, a defect inside the diamond lattice, which has attracted much attention due to its strong coupling to neighboring spins and long coherence time [11]. Many experimental papers report on the realization of coherent coupling between the electronic-nuclear spins [12], or electronic-electronic spins [13] of individual NV centers. However, to truly build a quantum register based on spin qubits in diamond, the coherent coupling needs to be scaled up to a larger number of qubits. One of the visions for scalable quantum registers would be to form a 2D array of defects (figure 1–1) thus creating a network of qubits. One of the challenges of this vision

is the short spatial length at which magnetic dipole interactions couple the NVs. About 10 nm is the distance reported for coherent coupling between two NVs [14], which is too close to optically distinguish them using standard diffraction-limited optical resolution techniques.

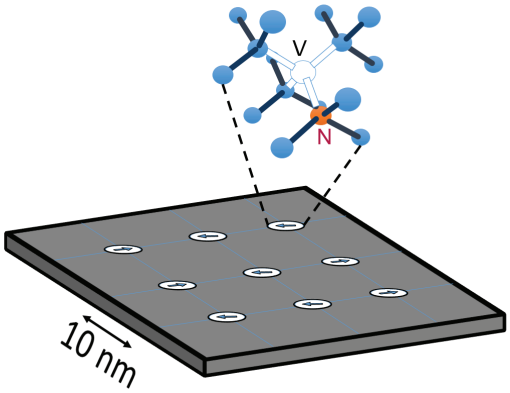

Figure 1–1: Scalable 2D quantum register based on the NV center. Each defect would be separated by about 10nm for the coupling strength to be relevant.

1.3 Stimulated emission depletion nanoscopy

To overcome this diffraction limit, the construction of a subwavelength imaging technique called stimulated emission depletion (STED) nanoscopy will allow detection of single defects only a couple of nanometers apart. For applications involving interacting spins, it is important to find out if the STED beam alters the spin state. Initial work has already been made investigating the influence of STED on the NV spins, showing that spin population could be preserved during STED readout, but that the spin coherence seemed to be destroyed [15]. However more work needs to be done to truly understand the effect of STED on interacting NVs. One aspect of this investigation is

understanding how STED affects the charge state of the NV center.

1.4 NV center charge state

The NV center possess two charge states, the negative NV^- and neutral NV^0. Transitions between these two charge states are possible through photo-induced excitation [16]. Some experiments have made use of these transitions, such as reading out the spin state of a single NV via spin-to-charge conversion [17]. However, for most applications, these transitions are undesirable because the interesting quantum information properties of the NV center are only present in the NV^- state. Making sure the NV center remains in its negatively charge state when using STED will be crucial for its potential use in quantum information applications.

1.5 Overview of the thesis

The following thesis describes initial work towards investigating the effect of STED nanoscopy on the charge state of the NV center. To address this goal we built a setup capable of resolving and controlling single NV spins at room temperature and extended it to charge state detection. The first section consists of describing the construction of a confocal microscope for the study and detection of defects in diamond. For the control of experimental sequences, the second part details the development of an arbitrary Pulse-Pattern Generator using a Field Programmable Gate Array (FPGA) card in a LabView environment. In the final section we measure the switching rates (Γ_- and Γ_+) associated with blinking induced by ionization of the NV center as well as obtaining a fidelity measurement for the charge state (NV^- and NV^0) detection of the NV center using a 594 nm laser.

CHAPTER 2
Introduction to the NV center

The NV center is a complex system that is probed through different means. The manipulation of the NV center spin states is made via electromagnetic waves at the MW frequencies. On the other hand, the detection and measurement of its various states is made through optical means. In this chapter, we consider the basic structure of the NV center and present experimental techniques used to probe its spin and optical transitions.

2.1 Atomic Structure of the NV center

Diamond is defined by a face-centered cubic crystal structure and possesses a basis of two carbon atoms. Imperfections can be found in the crystal lattice of diamond. These imperfections, usually referred to as defects, occur naturally during the growth process of a diamond sample. The nitrogen-vacancy center is one of many defects existing within the structure of diamond. The NV center is composed of two nearest neighbor carbon atoms substituted by a nitrogen atom and a vacancy. The absence of one carbon atom creates a system of dangling bonds between the nitrogen atom and 3 carbon atoms, which exhibits the C_{3v} point group symmetry [18].

It is possible to calculate the allowed electronic single electron orbital states of the defect by projecting the dangling bonds on each irreducible representation(IR) of the C_{3v} point group. The projection leads to four different

orthogonal orbitals. 2 are totally symmetric and non-degenerate and transform according to the one-dimensional IR A_1; meanwhile 2 are degenerate states that transform according to the 2D IR E. Understanding how valence electron fills up the possible allowed orbitals gives us more insight on the energy structure of the defect [18].

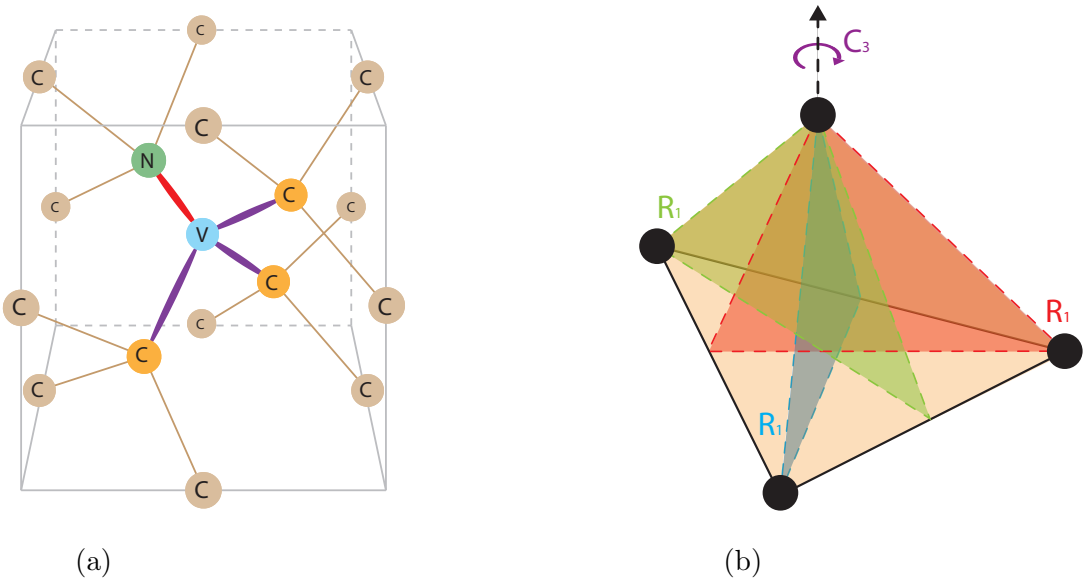

(a) (b)

Figure 2–1: a) NV center in diamond b) Symmetry operations of the C_{3v} point group; C_3 and C_3^{-1} are rotation by 2πn; R_1, R_2 and R_3 are reflections along the symmetry planes.

2.2 Electronic Structure of the NV center

The NV center possesses three electrons from dangling carbon bonds and two valence electrons from the nitrogen atom. It also has the possibility of acquiring an extra negative charge within the system leading to two different charge states NV^- and NV^0. This extra electron leads to a considerably different energy structure for the two charge states. The NV^0 posses a very short spin coherence times due to its ground sate orbital doublet undergoing fast dephasing through phonon interactions, which makes it an unappealing choice for quantum information applications. Also, although the NV^0 state

has recently shown some promising applications, notably in sub-diffraction imaging through charge state manipulation [19], it is the NV^- charge state energy structure that is promising for quantum information and magnetometry applications. The rest of this chapter will be looking exclusively at the NV^- properties.

The NV^- fluorescence spectrum (figure 2–2) is characterized by a sharp peak at 637 nm coming from a zero phonon line transition between its ground and excited state and a broader feature at longer wavelengths attributed to a phonon sideband [20].

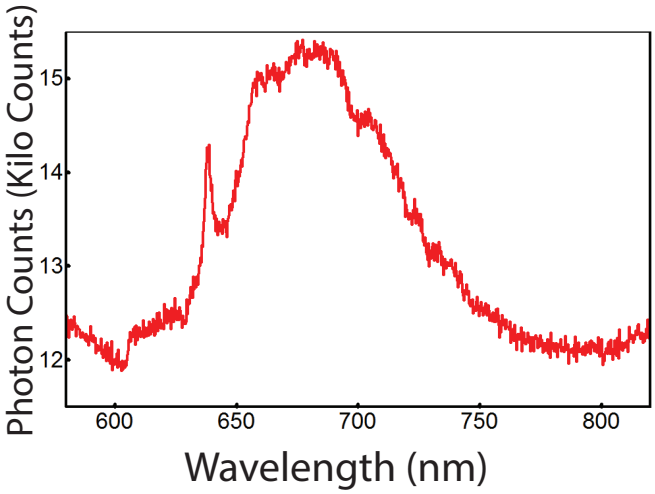

Figure 2–2: Emission spectrum of the nitrogen vacancy center at room temperature using a 532 nm excitation laser. A sharp peak at 637 nm is attributed to the zero phonon line transition and broader features in longer wavelength to the phonon sideband.

At room temperature the energy levels of the NV^- are comprised of a ground and excited state (figure 2–3). The ground state is a spin triplet with symmetry $^3A_2$ and its degeneracy is lifted by 2.87 GHz due to spin-spin interactions. It is described by an $m_s = 0$ state with symmetry A_1 as well as two $m_s = \pm 1$ states with symmetry E. There is a strong optical transition to an excited triplet state, with symmetry ^3E, that conserves spin. In addition to

the allowed spin preserving optical transitions via electric dipole interactions, the NV^- also possesses a non-radiative intersystem crossing to singlet states mediated by the spin-orbit interaction. This relaxation path starts in the excited state and goes through a set of metastable singlet states with A_1 and E symmetry before relaxing to the ground state [18]. This non-radiative transition is used for spin state initialization and readout of the NV^-.

Under green illumination (532 nm) the NV^- exhibits state initialization to the ground state $m_s = 0$ with fidelity ranging between 70% to over 90%. The spin polarization occurs because of the singlet state lying between the excited and ground state. Transitions to the singlet states occur mostly from the excited state $m_s = \pm 1$, while relaxation out of the singlets is not strongly spin-selective [21]. This loop effectively traps the majority of the spin population into the $m_s = 0$ optical transition.

It is also possible to distinguish the spin state of the NV^- center via its fluorescence. At room temperature, the $m_s = \pm 1$ state fluoresces up to 40% less than the $m_s = 0$ state [22]. This difference originates from the intersystem crossing transition which occurs primarily for the $m_s = \pm 1$ state. Since the decay time out of the singlet states is longer than the radiative lifetime of the excited state, the $m_s = \pm 1$ states spend on average less time cycling through the radiative transition, leading to an effective reduction of fluorescence counts. Looking at the time resolved luminescence (figure 2–4), the fluorescence rate of the $m_s = 0$ and $m_s = \pm 1$ spin states are differentiable until a certain critical time ($\approx 0.8\ \mu s$) where pumping to the $m_s = 0$ state renders the technique inefficient.

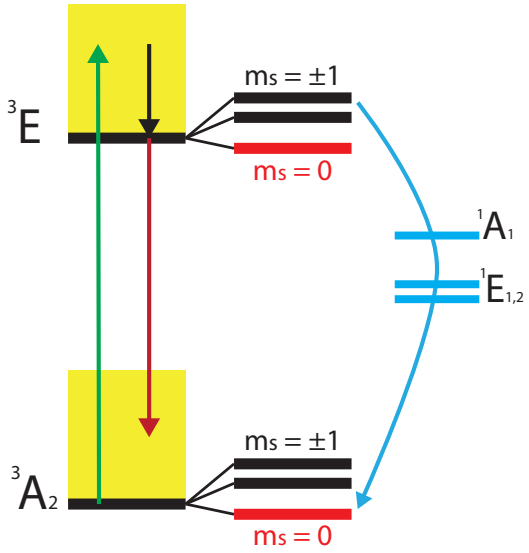

Figure 2–3: Nitrogen-vacancy center room temperature energy levels. The colored arrows represents the 532 nm excitation laser(green), the spontaneous fluorescence(red), the intersystem crossing transition(blue) and the phonon relaxation(black). The phonon sidebands of the ground and excited states are represented in yellow.

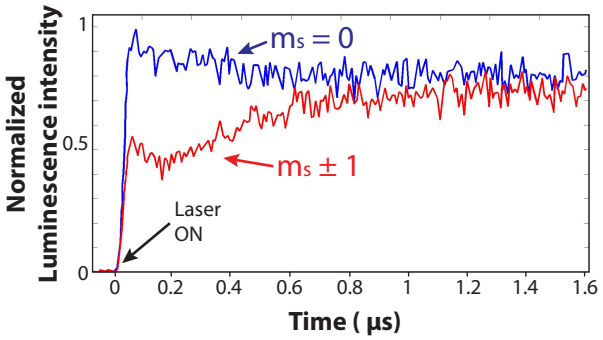

Figure 2–4: NV center time resolved luminescence with a 532 nm excitation laser. First, the spin state is prepared at either $m_s = 0$ and $m_s = \pm 1$ and a time trace of the fluorescence is then taken. Higher counts are measured from the $m_s = 0$ state until an equilibrium due to pumping is reached

The electronic structure of the NV center offers a quite unique playground for solid states applications. Its electronic structure is especially interesting for STED nanoscopy due to its large phonon sideband and stable optical transition.

2.3 Stimulated emission depletion nanoscopy

As stated in chapter 1, to go beyond the diffraction limit of conventional optical techniques, stimulated emission depletion (STED) nanoscopy can be used. STED can be used in a wide range of physical systems. The following section presents the use of STED more particularly for NV centers.

For NV center systems, a 532 nm laser is used as a centered gaussian beam and a 765 nm laser is used as a donut shaped outer beam (figure 2–5 a). Using STED the excited outer NV centers are forced back to the ground state by stimulated emission, effectively turning off their signaling capabilities. This occurs only if the stimulated emission rate is larger than that of the spontaneous decay, so that the outer NVs have no time to spontaneously fluoresce. This contrast in fluorescence differentiates the two types of NVs which will allows us to discern the two defects [23]. When scanning over the sample, only one nitrogen-vacancy center is situated at the center of the doughnut-shaped beam. All the outer NV centers are shut-off. The center area is allowed to emit and has a diameter :

$$\Delta d = \frac{D}{\sqrt{1 + \frac{I}{I_s}}} \tag{2.1}$$

where $D = \lambda/(2NA)$ is the spatial resolution, λ is the wavelength, NA is

the numerical aperture of the objective lens, I is the intensity of the doughnut crest, and I_s is the characteristic intensity that reduces the population probability of the fluorescent state of the NV center by half [24].

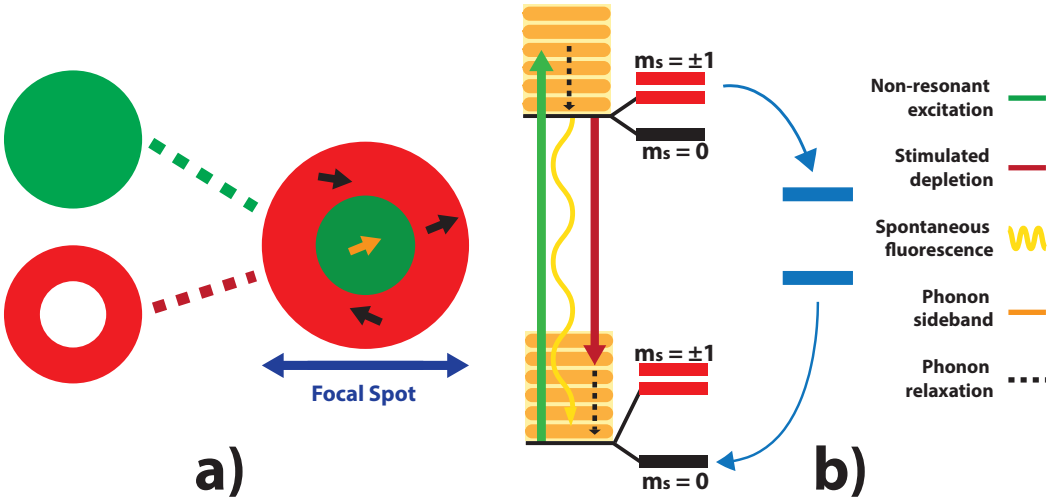

Figure 2–5: a) Superposition of the 532 nm excitation beam (green) and the 765 nm depletion beam (red) for STED b) Energy diagram showing the added stimulated depletion path (red arrow)

STED has shown very good results in identifying single NV centers and the current record provides a resolution down to 2.4±0.3 nm [25]. However, for this technique to be useful in a quantum register of closely spaced spins, one must understand what happens to the information stored in the outer defects while the center NV is being addressed. More specifically one must understand how a single NV center behaves under excitation-depletion cycles and how the cycles affect the electronic charge state and the polarization and coherence of electronic and nuclear spins.

Planned experiments will use Gaussian beams for both excitation and depletion lasers. Figure 2–6 shows a general pulse protocol to investigate the excitation-depletion cycles. First an excitation pulse is used to probe the NV center charge state, afterward a microwave pulse is applied for initializing the

electronic spin state to any superposition desired, third the excitation and depletion picosecond pulses are applied and finally we look at what happened to the charge and electronic spin state. The goal of this thesis is to show initial work to establish the first laser pulse of figure 2–6 sequence, which is measuring the charge state of the NV center.

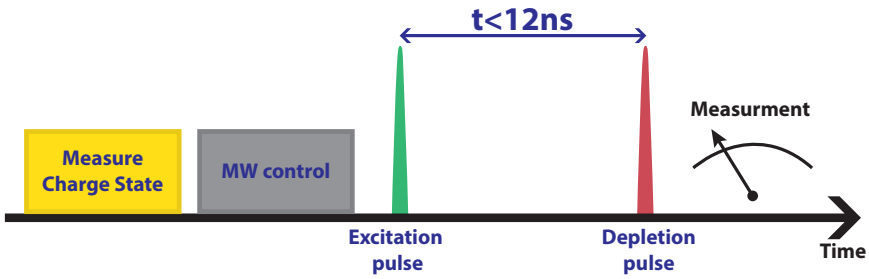

Figure 2–6: Pulse protocol for investigating the effect of STED on the NV center. First, the charge state of the NV center is measured. Second, MW pulses are applied to initialize the defect spin state. Third, STED pulses are applied. Finally, investigation of the charge state or the polarization and coherence of electronic and nuclear spins is performed.

2.4 Charge state ionization cycles

As written earlier, NV centers possess two stable charge states, the negative NV^- and neutral NV^0. Transitions between these two charge states are possible through photo-induced excitation [16, 26, 27]. Figure 2–7 reveals a simple ionization mechanism [28]. Using a 594 nm laser, transitions between the ground and excited state of the NV^- are induced. Over time, a two photon process is possible, where an electron from the defect is driven from the

excited state to the conduction band of the diamond, leading to an ionization to the NV^0 state. Recovery to the NV^- is done by optically exciting the NV^0 leading to the transfer of an electron from the valence band to the defect.

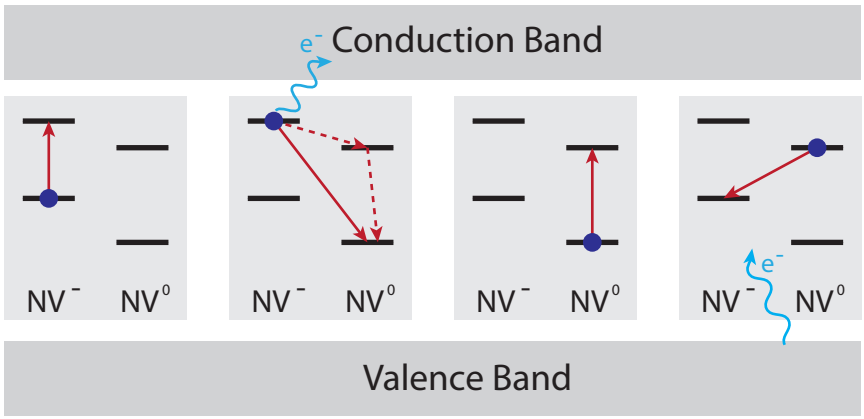

Figure 2–7: Above figure illustrates the NV center ionization process. First, the NV^- cycles between the ground and excited state using a 594 nm laser. Afterward, there is a probability of a two photon process occurring exciting one electron into the conduction band and ionizing the defect into NV^0. Recovery to the NV^- is done by optically exciting the NV^0 leading to the transfer of an electron from the valence band to the defect.

One way of discerning between the two charge states is by looking at their fluorescence levels using yellow light. When the defect is illuminated with a 594 nm laser, a cycling transition between the ground and excited state occurs and emitted light is scattered in the process. However the frequency of the yellow light excites the NV^- much more efficiently than the NV^0 leading to a higher emission rate than for the NV^0 state. This higher coupling leads to higher fluorescence counts for the NV^- and lower fluorescence counts for the NV^0, allowing us to directly differentiate between the two states.

CHAPTER 3
Experimental apparatus

One objective of this masters degree was to build a setup capable of resolving and controlling single NV spins at room temperature. The setup used is a confocal microscope which can be upgraded to utilize STED. Laser scanning confocal microscopes have been used in a broad range of applications, notably in the biological and medical sciences [29]. The principle of confocal microscopy is to use a focused light source to address the optical transition of an emitter and collect its fluorescence out of a pinhole,in our setup, the single-mode fiber replaces the pinhole. By scanning over the entire sample we are able to locate every emitter and a confocal image is built up pixel by pixel.

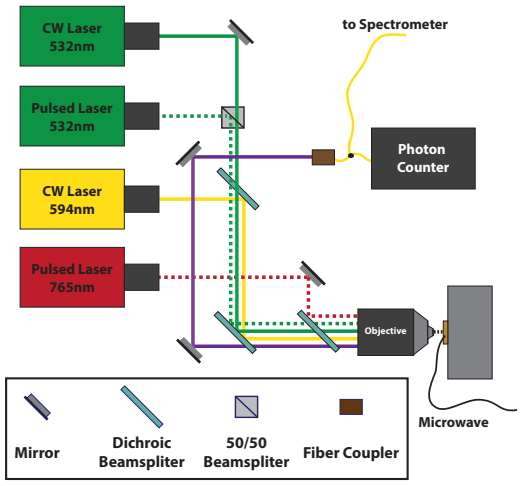

Figure 3–1: Illustration of a confocal microscope with 4 different excitation lasers.

A home-built confocal microscope was used for the detection of the NV centers' photoluminescence. There are 5 major components to our confocal microscope : the coherent light source, the dichroic mirrors, the objective lens, the sample mount and the fluorescence collection.

3.1 Coherent light source

3.1.1 Lasers

We use a 531 nm green LDH Series Picosecond Pulsed Diode Laser Heads from PicoQuant at 80 Mhz repetition rate for probing the NV^-. The pulsing of the green laser will be relevant when STED nanoscopy will be incorporated into the setup. Otherwise, the pulsed laser functions as a continuous laser for the purpose of our experiments. For the charge state detection experiments the R-39582 HeNe yellow laser from Newport at 594 nm emission and 2 mW output power is used.

3.1.2 Modulation

For controlling the frequency and the power of our laser beams, acousto-optical modulators (AOMs) were used. For the 531 nm green laser, we use the 15210 AOM from Gooch & Housego with 0.65 μs delay time and 0.05 μs rise time. For the 594 nm yellow laser, we use the 1250C AIM from ISOMET with 0.891 μs delay time and 0.05 μs rise time.

AOMs are composed of a transparent crystal to which is attached a piezo-electric transducer used to generate sound waves inside the crystal at frequency on the order of 100 MHz. The generated sound waves induce a periodic refractive index grating inside the crystal and when light passes through the crystal,

Bragg diffraction is observed in the output of the AOM. Usually the first order diffracted beam is then isolated from all other beams and acts as primary light source. The power and frequency of the first order diffracted beam can then be directly controlled by how much the piezoelectric transducer is driven [30].

The piezoelectric transducer is driven by an electrical radio frequency (RF) signal provided by the AOM driver. The AOM driver is made up of four components (figure 3–2), a Voltage Controlled Oscillator (VCO), a Voltage Variable Attenuator (VVA), a switch and an amplifier. The VCO outputs a RF signal necessary to drive the AOM. The VVA attenuates the VCO's output, the amount of attenuation is varied by the voltage control input of the VVA. The Switch turn On/Off the microwave signal via a TTL pulse signal. The amplifier amplifies the output of the VVA, such that the RF output is sufficient to drive the AOM. The response of the AOM varies with the frequency and amplitude of the input RF signal.

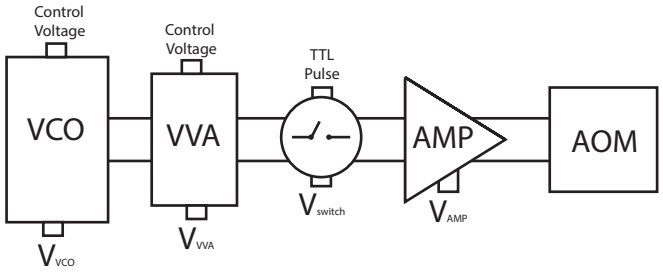

Figure 3–2: A home built AOM driver circuit composed of a Voltage Controlled Oscillator (VCO), a Voltage Variable Attenuator (VVA), a switch and an amplifier.

When a laser beam passes through a turned off AOM, some background light can be measured through the 1st order path. To reduce the effect of this unwanted residual light, an AOM in the double-pass configuration can be used (figure 3–3).

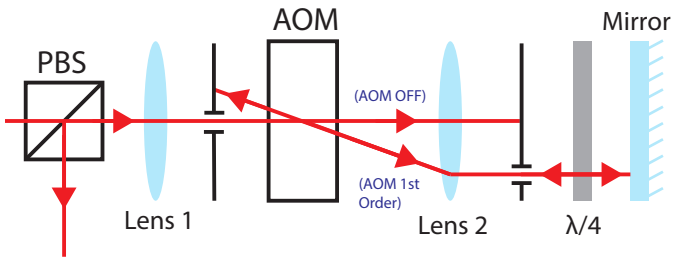

Figure 3–3: An AOM double pass configuration; the laser beam is first focused into an AOM by lens 1; the AOM 1st order is picked out and collimated by lens 2; a quarter-wave plate and a mirror turn the laser beam polarization by 90°; the beam is diffracted again on the second pass, which then returns along the same path as the input beam; a polarizing beamplitter cube separates the path of the initial and final beam.

3.1.3 Spatial filter

Due to the point source or from passing through the AOM system, a laser beam mode quality might be imperfect. A spatial filter composed of two lenses and a pinhole can be use to "clean up" the mode quality of the laser beam.

The pinhole is aligned at the focal plane of the first lens, where different spatial Fourier components of the original beam are spatially separated. The pinholes blocks the off-axis components of the beam that do not focus on the

center hole and the output beam has a airy intensity profile, which is associated with a "cleaned" phase profile. The second is used to collimate back resizing the beam. The size of the beam should be large enough to fill up all of the exit pupil of the objective equal to $2 \cdot f \cdot NA$ [31].

3.2 Objective lens and focusing spot

For imaging defects in diamond, we use the Olympus UPLANSAPO 60X/1.35 oil immersion objective. The choice of the objective lens is extremely important, as the collection efficiency, which scales as the square of the numerical aperture ($\sim NA^2$), depends on it. Also, the image resolution of the defect will depend mostly on the beam waist after being focused by the objective lens. For a gaussian beam, the minimum focal spot size d_o is given by :

$$d_o = \frac{2\lambda}{\pi NA} \tag{3.1}$$

where λ is the light wavelength and NA is the numerical aperture of the lens. We see that the spot size is inversely proportional to the NA of the objective, hence the importance of getting a high NA objective lens. The NA of an objective lens is defined by :

$$NA = n \sin \theta_D \tag{3.2}$$

where n is the index of refraction of the medium and θ_D is the half-angle of the maximum cone of light that can enter or exit the lens. Getting high NA is specially important when imaging through diamond due to the effect of refraction. When imaging into diamond, the collection angle θ_D is reduced to θ_{eff} which effectively reduces the NA of the objective lens (figure 3–4). It is difficult to achieve NA values above 0.95 with dry objectives and higher

NA apertures can be obtained by choosing a higher refractive index medium between the specimen and the objective front lens. Oil immersion lens are usually a good solution because they routinely achieve a NA of about 1.40.

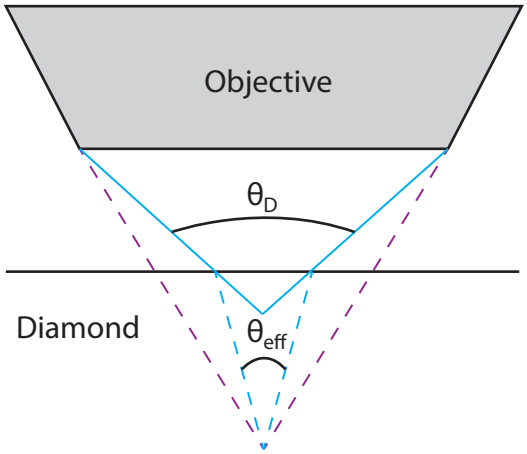

Figure 3–4: Change in the collection angle and focused point of an objective when imaging through diamond.

Another important aspect to take into consideration when choosing a proper objective lens are aberrations. Usually an objective lens is composed of a multiple set of lenses to compensate for optical aberrations such as spherical aberrations and field curvature. Chromatic aberration corrections are also a parameter to consider when building a optical setup with broadband emitters involved. The highest level of correction is found in apochromatic objectives. They offer spherical aberration correction and are corrected chromatically for 3 to 4 colors, making them the best choice for a future STED setup [32].

3.3 Dichroic mirrors

Dichroic mirrors are mirrors with transmission and reflection properties that depend on the light's wavelength. Usually, a cut-off wavelength sets what

part of the spectrum is reflective or transmissive. Dichroic mirrors are used to merge excitation beams together, as well as isolating the fluorescence path from the excitation beams. We are using a 550 nm short-pass mirror for merging the green and yellow excitation beam and a 635 nm long-pass mirror for isolating the fluorescence path (figure 3–1).

Dichroic mirrors are usually made up of multiple layers of thin-film coated on a glass substrate. The drying process of the coating can induce intrinsic stress which cause bending to the glass substrate. This bending has little effect on the trajectory of the transmitted beam. However, reflected light can be significantly impacted by a bent filter substrate.The flatness of the dichroic mirror will be significantly important when incorporating the STED depletion beam into the setup. A highly flat dichroic mirror is required for not altering the quality of the donut shaped depletion beam.

3.4 Sample and stage mount

A 1x1x0.2 mm chemical vapour deposition (CVD) grown diamond was used for all experiments. The sample was mounted on a 3-axis NPXY100Z25-219 nanopositioning stage from npoint, with 100 μm range on the x-y plane and 25 μm range on the z axis. The nanopositioning stage is controlled via three analog inputs ranging from -10V to 10V.

Because the sample is too small for micro-fabrication, a simple copper wire was placed on top of the sample as a microwave guide. A Rohde and Schwarz SMIQ03B Signal Generator (300 kHz-3.3 GHz) was used as a microwave generator.

3.5 Fluorescence collection

The fluorescence is focused by an Olympus UPlanFL N 4X PhP objective into a single mode fiber. The fiber is then connected to a single photon counting module. A BLP01-635R-25 635 nm long-pass filter from Semrock was used in front of the objective to block unwanted light attributed to Raman scattering observed at 645 nm from the yellow laser.

3.6 Future upgrades

For STED to be implemented into the setup, a new depletion path will need to be incorporated into the confocal microscope. This depletion path will include a 765 nm pulsed laser as a source and a number of optical elements described above, such as an AOM and dichroic mirror. It will also include a new component, essential to the formation of the doughnut shaped beam, called a vortex phase plate. When the depletion beam passes through the vortex phase plate, a helical phase ramp of 2π is imprinted onto the wavefront. Afterward, the beam is focused by an objective lens and the field will interfere destructively in the center of the focus, leaving a doughnut shape at the focal plane [33].

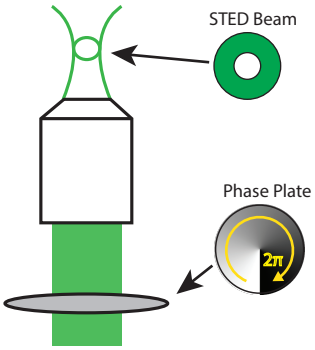

Figure 3–5: Illustration of a STED beam created using a vortex phase plate. A helical phase ramp of 2π is imprinted onto the wavefront when the laser beam passes through the vortex phase plate. This phase ramp creates a doughnut shape beam because of the field interfering destructively into the center.

CHAPTER 4
Software implementation

In addition to the experimental apparatus, the software implementation needed to be built from scratch. The readout and control of the NV center's many states requires management of fast pulse signals. For example, the photon detector pulses are about $\sim$ 15-20 ns long and and separated by a dead time < 70 ns. Making sure we count all photons detected thus requires a fast clock cycle in the range of 100 MHz. Also, Rabi oscillation frequencies of the NV center can be measured in the 10-100 MHz range. To gain control over the spin degrees of freedom, fast gates over the MW lines need to be set for establishing proper π-pulses (Appendix A contains examples of pulse protocol using the FPGA for spin manipulation of the NV center).

For the control of experimental sequences a Pulse-Pattern Generator (PPG) has been developed based on a Field Programmable Gate Array (FPGA) addressed in a LabVIEW environment [34]. The PPG allows for the control of 14 digital Inputs/Outputs (DIO) with highly reproducible clock cycle of 120 MHz as well as 8 Analog Outputs (AO).

4.1 FPGA card

We needed a good implementation of fast logic and input/output (I/O) interface for data processing. An FPGA card is the solution we implemented.

FPGAs are reprogrammable silicon chips commonly used in embedded system applications because of their complex I/O interfaces and in-stream data processing.

For a better understanding of the PPG software implementation, it is important to understand what are the FPGA card capabilities and internal components. All FPGAs are composed of five basic parts described below [35] :

1. Configurable Logic Blocks (CLBs) are the basic logic unit of an FPGA. They are made up of two basic logic gates : flip-flops and lookup tables (LUTs). The LUTs are flexible enough to handle combinatorial logic, shift registers or RAM. For example, the logic for counting photons is made up of CLBs.

2. I/O Blocks allows connections with outside instruments. The FPGA currently handles DIO with TTL logic as well as 32-bit AO ranging from -10 V to 10 V. Instruments needing fast logic gates, such as the MW line switch and the photon counter, were connected to these I/O blocks.

3. Block RAM Memory is available in FPGAs allowing for on chip memory design. Flash storage is not available in FPGAs, meaning they have very little storage capabilities and need to be reconfigured every time power is reset.

4. Programmable Interconnects provide the routing between the CLBs, the I/O blocks and the RAM. The flexibility of the FPGA's functionality comes from the reprogrammability of these interconnects, allowing for

application specific hardware programs.

5. Digital Clock Manager (DCM) deals with all aspects of clock management. The DCM provides precise clock locking as well as advanced clocking capabilities to multiply or divide the incoming clock frequency to a new one. For example the PPG currently runs at a clock of 120 MHz which is 3 times the base clock frequency of 40 MHz of the FPGA card.

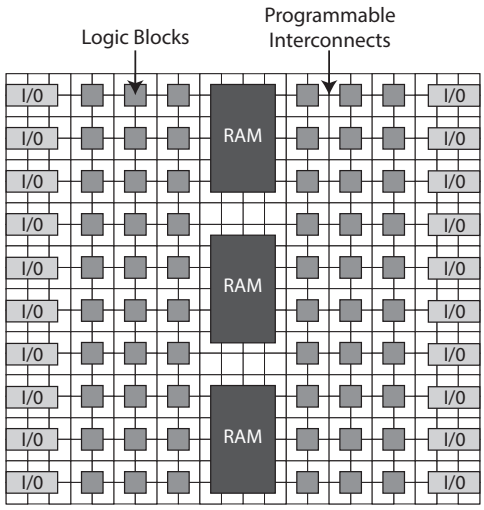

Figure 4–1: The different parts of an FPGA

4.2 Host and Target VI relationship

As seen in the last section, FPGAs do not have the memory capabilities to handle complex functions. Other essential tasks such as handling large arrays or saving data to a disk are also not possible using an FPGA. As a result, a hybrid architecture where an external processor that is paired to an FPGA card that is then connected to I/O has been the most favored solution for companies developing FPGA cards, such as Xilinx. In addition, to avoid

difficulties of FPGA programming languages, we used a Labview package to implement our software.

For our applications, we decided to use such a hybrid system, where a Host computer is connected to an FPGA card, which is then connected to the I/O of the optical table (figure 4–2). Two Labview codes, one controlling the host computer and called the Host VI and one controlling the FPGA and called the Target VI, are continuously running and talking to each other.

The role of the Host VI is to perform any complex operations which are too memory-consuming for the FPGA. It is responsible for writing the pulse pattern into the FPGA as well as retrieving raw data sent by the FPGA and saving it to the disk. The Host VI also provides the user interface to communicate with the FPGA card.

The Target VI role is to retrieve data from the Host VI and create the pulse pattern for the optical table devices. The voltage pulses coming from the photon counter are also read by the target VI and transformed into a digital number which is then sent to the Host VI.

Figure 4–2: 1. Target VI retrieve the pulse pattern information from the Host VI; 2. Target VI create the pulse pattern for the optical devices; 3. Target VI counts pulses coming from the photon counter; 4. Photon counts are sent to the Host VI and saved

4.3 Target VI architecture

For the control of all experimental I/O, a pulse-patten generator has been developed based on an FPGA code addressed in a LabVIEW environment called the Target VI. The Target VI currently communicates with 15 different DIOs as well as 8 AOs. Due to very deterministic timed loop, the DIOs can be read or set every clock cycle of the FPGA card, i.e. every 8.3 ns. On the other hand the AOs can only be reset every cycle of the Target VI, which depends on the timing of the pulse sequence and the Host computer timing (see Appendix B for details on Target VI cycle time).

The reproducible clock cycle of the DIOs is due to a loop structure only present in the target VI called a timed loop. Any command written inside this timed loop must be completed within the clock cycle of the timed loop

otherwise the code will not be compiled. A single target VI can contain multiple timed loops, however every timed loop must have the same clock cycle or again the code will not compile. For our current applications, the timed loop clock cycle has been set at 120 MHz. Writing different states into the DIOs is fast enough for them to be contained inside a timed loop. Unfortunately it is not the case for AOs and the architecture of the target VI has been designed based on that restriction.

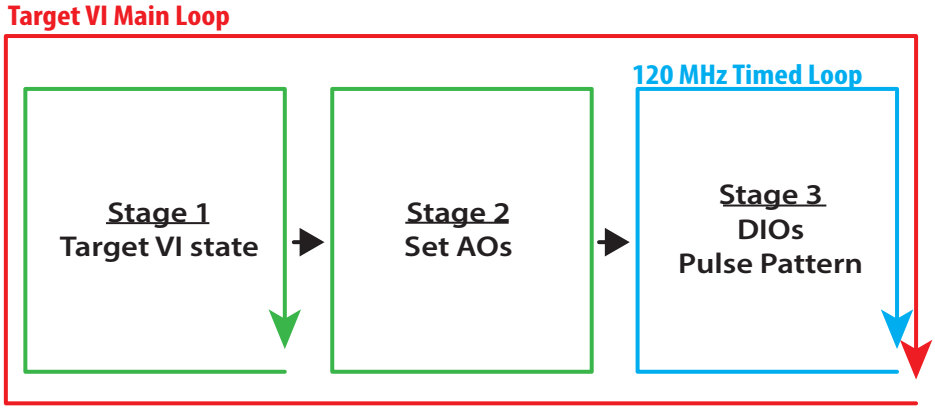

Figure 4–3: The target VI sequence

Communication with the Target VI is done via five I/Os presented in table 4–1 and the higher level of the Target VI possesses 3 stages (figure 4–3) that are explained below:

1. Target VI state : First a boolean control sets the state of the target VI. A Fasle value of the Boolean control instructs the target VI to remain idle, a True value instructs the target VI to pass onto the second stage.

2. AOs states : The second stage sets the AO voltages. Since the AOs are reset once every cycle of the target VI loop, their states are controlled through eight unsigned 32 bit (U32) scalar controls.

3. DIOs Pulse Pattern : The third stage applies a pulse pattern to the DIOs and reads the fluorescence counts. For the DIOs more information needs to be manipulated and the data is transferred via U32 1D arrays called Direct Memory Access (DMA) channels. The elements of the DMAs are read through a First in First Out (FIFO) method. The DIO pulse pattern runs through three parallel loops and uses two DMAs channels plus two on-board FIFOs. (figure 4–4). The Host to Target DMA is used to transfer the pulse pattern to the DIOs. However the Target to Host DMA is not fast enough for the 120 MHz timed loop and an intermediate Target Scoped FIFO has to be used inside the timed loop to set the state of the DIOs. The same goes for writing fluorescence counts to the Host VI : an intermediary Target Scoped FIFO has to be used before transferring the counts to the Target to Host DMA.

Input name	Type	I/O	role
start	Boolean scalar	Input	control the idle state of the target VI
AO0(to 7)	7 U32 scalars	Input	control the state of the AOs
HtoT	1D U32 array	Input	pulse pattern of the DIOs
delay	U32 scalar	Input	delay between the AOs and the DIOs
TtoH	1D U32 array	Output	fluorescence counts

Table 4–1: All target VI inputs. These inputs cannot be modified directly from the target VI. Values of the inputs are modified from the Host VI and sent to the target VI through the Host to Target DMA.

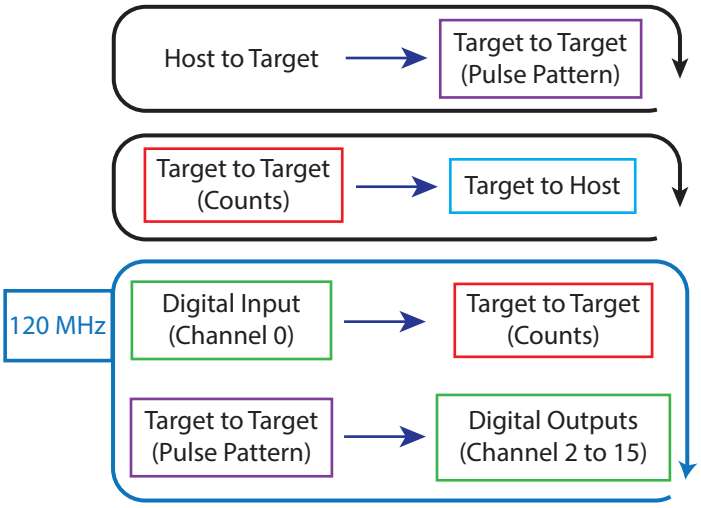

Figure 4–4: The DIOs pulse pattern data flows through 3 different loops. Loops 1 and 2 are used to transfer data in and out of the 120 Mhz timed loop (loop 3), via the Target to Target FIFOs. Loop 3 is the main loop writing the pulse into the DIOs (green squares). DIO channel 0 is the counting input and is used only for acquiring the counts received from the photon counter. DIOs channel 2 to 15 are used for outputting any random pulse pattern. DIO channel 1, which is not illustrated, controls the timing of the counting intervals.

4.4 Host VI architecture

The Host VI is run by the local computer and its role is to communicate orders to the Target VI, save data from target VI to disk and perform more complex analysis with the data.

4.4.1 Communicate orders to the Target VI

As explained in last section, communication with the Target VI is done via five different I/O variables presented in table 4–1. Because of limited memory inside the FPGA, the data flow had to be managed meticulously. The AO information does not require a lot of space as the controls are only scalars, however the DIO pulse pattern information needs to be compressed. Figure

4–5 shows the first step of how the DIOs pulse pattern data, written from the Host VI, is transformed.

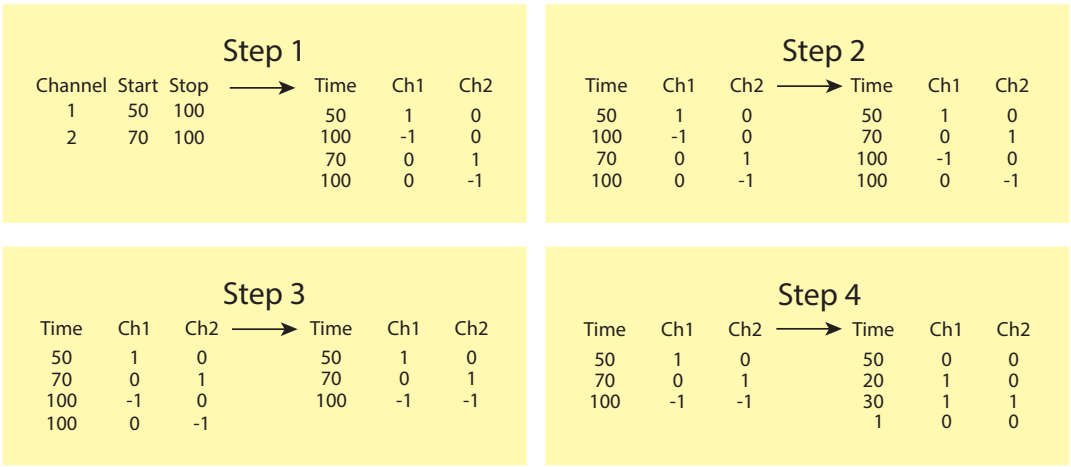

Figure 4–5: Exemple values for the pulse pattern data transfromation. Sequence 1: Events are grouped in terms of the time stamp, values of 1 and -1 are given to starts and stops respectively; Sequence 2: Time stamps are arranged in chronological order; Sequence 3: Similar time stamps are clustered together; Sequence 4 : Time stamp is written in terms of time difference

Since a 2D matrix containing a time stamp and the state of every DIO would overload the FPGA's memory, a second transformation is done where the time stamp and the DIOs states are embedded together. The mixing is done by writing the U16 time stamp into an array of its constituent bits and the 16 DIOs into another array of 16 bits and combining them into a U32 number (figure 4–6).

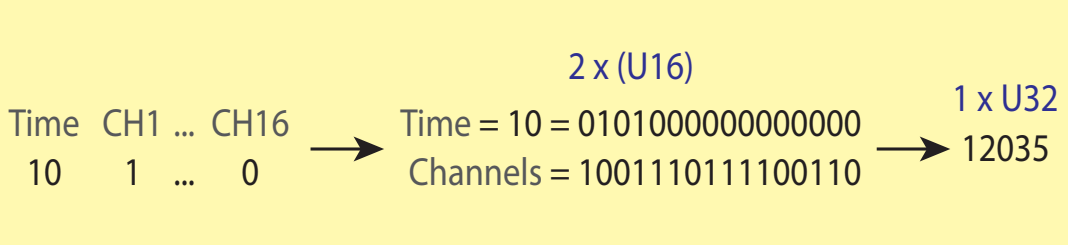

Figure 4–6: The illustration shows how the time stamp and channel states are embedded together. Time stamp and channels are written in terms of 16-bit; they are then grouped together to form a 32-bit scalar

4.4.2 Saving data from the Target VI

Many of the experiments in the lab require repetition of a certain pulse pattern many times for building up statistics. The duty cycle, which is the percentage of time in which data acquisition is active, then becomes very important for minimizing the overall time of an experiment. A key factor for minimizing the duty cycle is the time required for saving raw fluorescence counts to disk (figure 4–7).

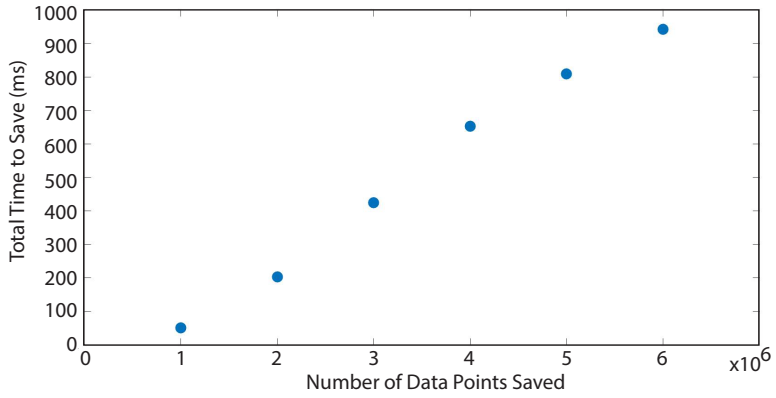

Figure 4–7: The total time to save to disk before implementing the parallel saving approach. We see that it takes a significant amount of time to save to disk and that the delay increases linearly with the number of data points. Each data point corresponds to a single fluorescence count.

To reduce the saving time, a parallel saving approach has been incorporated where data from the previous cycle is being saved to disk while the next cycle is running. This method minimizes the impact of saving to disk. The pulse patterns used for this thesis were all longer than the saving times which effectively neutralized the effect of dead time due to saving.

4.4.3 Data Analysis

Scanning, saturation curves and optimization are the tools currently contained in the The Host VI for acquiring raw data from the Target VI. They are contained inside a special LabView structure (called an event structure) which allows the Host VI to remain idle until one of the tools is activated by a control button.

1. Scanning : The scanning tool allows you to create a 2D intensity graph of an area of the sample (figure 4–8). It works by applying voltages ranging from -10 to 10 V via AOs sent to three ports of a nanopositioning stage which translate the voltages into an XYZ position. Because of the finite response time from the nanopositioner, a delay must be added between the AOs voltages and the counting to let the position stabilize.

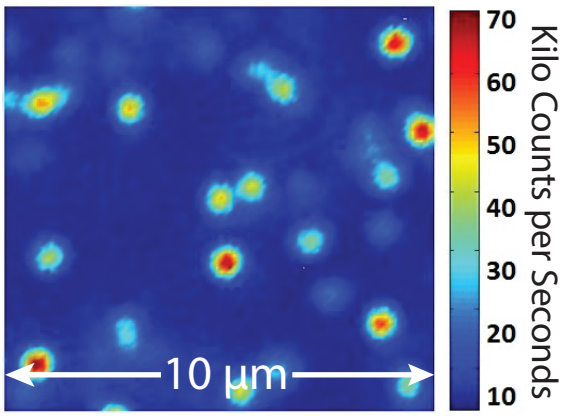

Figure 4–8: Scanning over the sample result in an intensity map of the photon counts. Each bright spot reveals the location of an NV center

2. Saturation curve : The saturation curve tool functions very similarly to the scanning. It works by applying voltages ranging from 0 volts to V_{eff} via an AO to an AOM. V_{eff} is the voltage at which the AOM lets the maximum laser power through. The laser power coming out of the AOM is dependent on the input driving voltage which allows measurement of the fluorescence count dependence on the laser power (figure 4–9), which follows equation 4.1 :

$$F = F_s \frac{P}{P_s + P} \tag{4.1}$$

where P is the power, P_s where half the saturating fluorescence is reached and F_s is the saturating fluorescence.

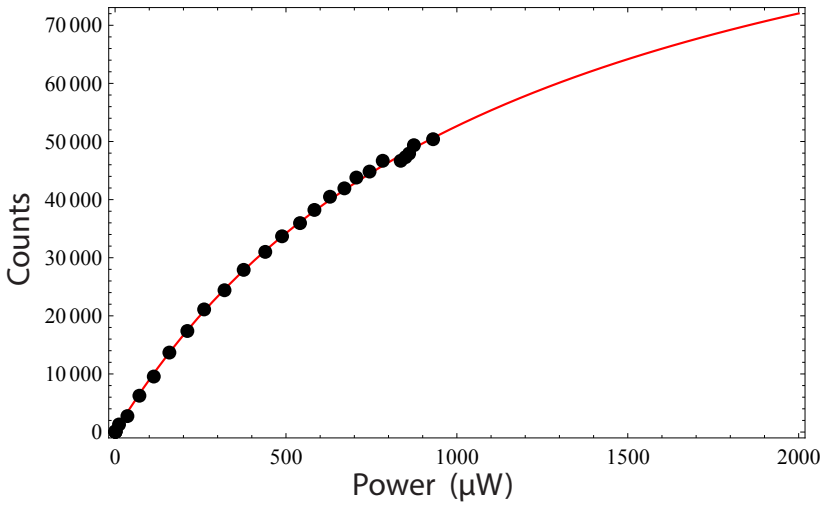

Figure 4–9: Saturation curve using a 594 nm laser. The saturation power couldn't be reached with the laser due to insufficient maximum power.

3. Optimization : Over long periods of time the nanopositioner may drift from its initial position which results in a laser focus point not centered on the studied defects and leads to lower fluorescence counts. The optimization tool re-calibrates the laser focus point onto the center of the studied defect, which is essential for long acquisition time experiments.

CHAPTER 5
Results and Analysis

The following chapter reports observation of cycles in the charge state of the NV center due to ionization from constant illumination with a 594 nm laser.

5.1 Isolating a Single NV Center

Measurements were performed on two different single defects (figure 5–1 a). To verify that these two defects are single NVs we performed a photon antibunching experiment. A beam splitter was used to separate the NV fluorescence. The separated beams were connected to two photon counters. The signal of the photon counters are then connected to a time-correlated single photon counting system (PICOHARP 300) through sma cables. One of the sma cables is longer than the other to induce a delay on the signal sent to the PICOHARP 300. The PICOHARP 300 then counts the number of times a delay of time τ is measured between the signals of photon counter 1 and photon counter 2. If the emitter is a single photon emitter, zero occurences should be counted for a zero delay between the two photon counters signals. This is equivalent to measuring the second order correlation function, in the limit of low count rates [36] :

$$g^{(2)}(\tau) = \frac{\langle I(\tau)I(0)\rangle}{|\langle I\rangle|^2} \tag{5.1}$$

where I(τ) is the fluorescence intensity at time τ. According to single photon

emitter statistics, $g^{(2)}(0) < \frac{1}{2}$. According to figure 5–1 b) and c) we measure $g^{(2)}(0) < \frac{1}{2}$ confirming the single emitter nature of the studied defects.

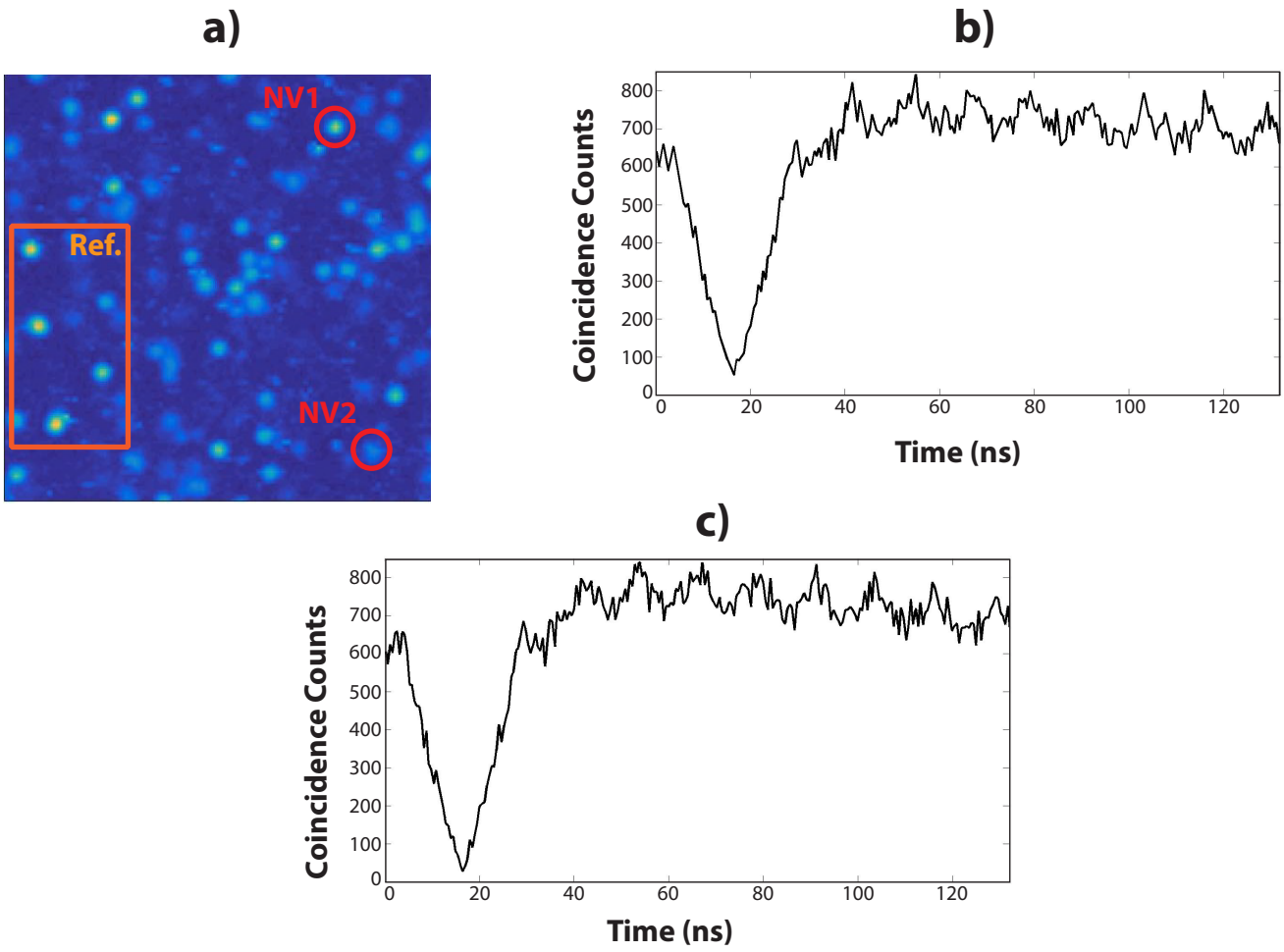

Figure 5–1: a) An Intensity map reveals location of the two NV centers used for this study. The four brights spots in the orange square were used as reference points for relocating the NV centers. b) Time-correlated single photon histogram for NV1 with $g^{(2)}(0) < \frac{1}{2}$ revealing it is a single NV. c) Time-correlated single photon histogram for NV2 with $g^{(2)}(0) < \frac{1}{2}$ revealing it is a single NV

The pulse sequence used for the experiment is illustrated in figure 5–2. First, a 594 nm yellow laser is turned on for 30 s while resulting fluorescence is counted in bins of 100 μs. A dead time of 8.3 ns separates each counting

periods. A 532 nm green laser is then turned on for 50 ms to make sure the defect is maximally aligned.

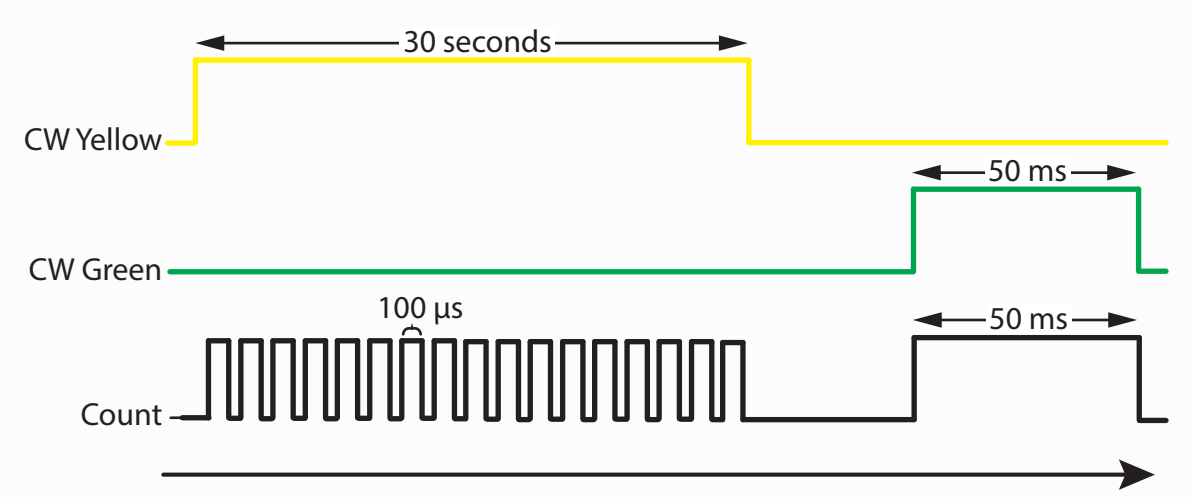

Figure 5–2: NV center charge state experiment pulse protocol

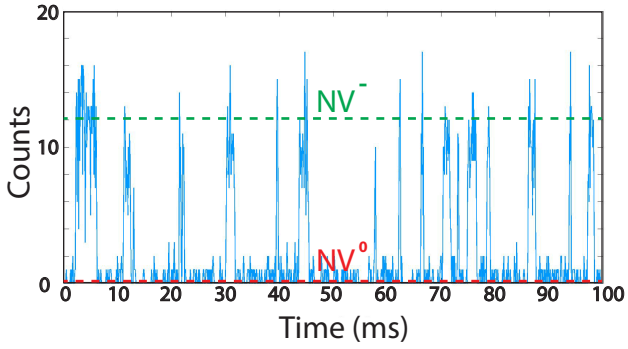

Figure 5–3: Time traces of the fluorescence using a 594 nm laser at 2 uW reveals cycling transition between the NV^- and NV^0 charge states . High counts correspond to NV^- state and low counts correspond to NV^0 state

During the yellow illumination part of the pulse sequence, cycling transition between the NV^- and NV^0 charge states are visible by looking at the fluorescence acquired. The 594 nm laser excites the NV^- states much more

than the NV^0 state resulting in higher fluorescence counts for the NV^- state (figure 5–3).

5.2 Ionization Rates

Extracting the transition rates (Γ_+, Γ_-) between the NV^- and NV^0 charge state is important before establishing a charge state measurement sequence.

5.2.1 Extracting the ionization rates

Here we present a model using the correlation function of a random telegraph signal to extract the ionization rates. Let ρ_+ be the probability to be in charge state $|+\rangle$ and ρ_- the probability to be in charge state $|-\rangle$. These probabilities obey the rate equations :

$$\begin{pmatrix} \dot{\rho_+} \\ \dot{\rho_-} \end{pmatrix} = \begin{pmatrix} -\Gamma_+ & \Gamma_- \\ \Gamma_+ & -\Gamma_- \end{pmatrix} \begin{pmatrix} \rho_+ \\ \rho_- \end{pmatrix} \tag{5.2}$$

We rewrite this in state vector notation :

$$|\dot{\rho}\rangle = L\,|\rho\rangle \tag{5.3}$$

where :

$$|\rho(t)\rangle = \begin{pmatrix} \rho_+(t) \\ \rho_-(t) \end{pmatrix} \quad ; \quad L = \begin{pmatrix} -\Gamma_+ & \Gamma_- \\ \Gamma_+ & -\Gamma_- \end{pmatrix} \tag{5.4}$$

Suppose that the initial state is $|\rho(t_0)\rangle$ at time t_0. Then the state at times $t > t_0$ is :

$$|\rho(t)\rangle = e^{L(t-t_0)}\,|\rho(0)\rangle \tag{5.5}$$

The probability that the charge state at time t is $|\chi\rangle$:

$$P(\chi, t) = \langle\chi|\rho(t)\rangle = \langle\chi|e^{L(t-t_0)}|\rho(t_0)\rangle \tag{5.6}$$

where $|\chi\rangle$ is either $|+\rangle$ or $|-\rangle$:

$$|+\rangle = \begin{pmatrix} 1 \\ \\ 0 \end{pmatrix} \quad ; \quad |-\rangle = \begin{pmatrix} 0 \\ \\ 1 \end{pmatrix} \tag{5.7}$$

Likewise, the probability that the charge state is χ_1 at time t_1 and χ_2 at time t_2 is, according to Bayes' rule and equation 5.6 :

$$P(\chi_2, t_2; \chi_1, t_1) = P\,\langle\chi_2, t_2|\chi_1, t_1\rangle\,P(\chi_1, t_1) = \langle\chi_2|e^{L(t_2-t_1)}|\chi_1\rangle\,\langle\chi_1|e^{L(t_1-t_0)}|\rho(t_0)\rangle \tag{5.8}$$

Let $A_\pm$ be the two respective signal levels for the charge states $|\pm\rangle$. The two-time autocorrelation function is then :

$$\langle n_2(t_2)n_1(t_1)\rangle = \sum_{\sigma\eta} P(\sigma, t_2; \eta, t_1)A_\sigma A_\eta \tag{5.9}$$

where the sum is over all possibilities for the charge states at time t_1 and t_2. We see that if we can calculate the probabilities of 5.8, we can obtain the autocorrelation function. Fortunately, L is a 2X2 matrix and can be exponentiated

exactly :

$$e^{Lt} = \frac{1}{\Gamma}\begin{pmatrix} \Gamma_- + \Gamma_+ e^{-\Gamma t} & \Gamma_-(1-e^{-\Gamma t}) \\ \Gamma_+(1-e^{-\Gamma t}) & \Gamma_+ + \Gamma_- e^{-\Gamma t} \end{pmatrix} \tag{5.10}$$

with $\Gamma = \Gamma_+ + \Gamma_-$. Now we can use these matrix elements to calculate equation 5.8. We assume that the initial state is the steady state :

$$|\rho(t_0)\rangle = \frac{1}{\Gamma}\begin{pmatrix} \Gamma_- \\ \\ \Gamma_+ \end{pmatrix} \tag{5.11}$$

Inserting 5.10 and 5.11 in 5.8, we get the probabilities. Then inserting the probabilities into 5.9 we obtain (after lots of simplifications) :

$$\langle n_2(t_2) n_1(t_1)\rangle = (\frac{\Gamma_-}{\Gamma}A_+ + \frac{\Gamma_+}{\Gamma}A_-)^2 + \frac{\Gamma_+\Gamma_-}{\Gamma^2}(A_+ - A_-)^2 e^{-\Gamma(t_2-t_1)} \tag{5.12}$$

where the first term is just the square of the steady state average signal. We can rewrite 5.12 as :

$$\langle n_2(t_2) n_1(t_1)\rangle = K_0 + K_1 e^{-\Gamma(t_2-t_1)}. \tag{5.13}$$

where :

$$K_0 = (\frac{\Gamma_-}{\Gamma}A_+ + \frac{\Gamma_+}{\Gamma}A_-)^2 \quad K_1 = \frac{\Gamma_+\Gamma_-}{\Gamma^2}(A_+ - A_-)^2 \tag{5.14}$$

We see that calculating the auto correlation function of luminescence traces of the NV center under yellow illumination will give us an exponential decay following 5.12. From fitting the values K_0,K_1 and Γ will be extracted. Values

for A_+ and A_- will be obtained by measuring the average count rates of NV^- and NV^0. We will then extract the rates Γ_+ and Γ_-.

5.2.2 Data

Fluorescence from yellow excitation has been registered for laser powers ranging from 0.55 μW to 5 μW and time traces of the fluorescence are shown in figure 5–4. The NV center charge states are well represented by the traces, where high counts correspond to the NV^- state and low counts to the NV^0 state. The increase of ionization rates with laser power are also observable from the traces as more switching is observable with increasing power and for the same window of time. Previous experiments have shown an $\sim I^2$ relation between ionization rates and laser intensity [16], where I is the laser intensity. This quadratic relation is explained by an ionization process originating from a two photon process, where an electron from the higher orbitals of the excited state is excited again with enough energy into the conduction band of the diamond.

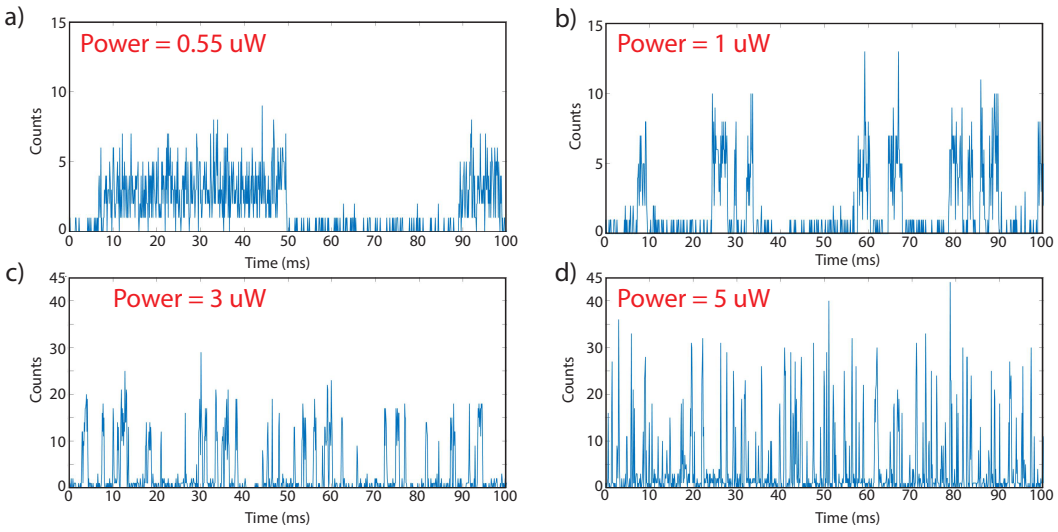

Figure 5–4: Time traces of the fluorescence using a 594 nm laser reveals higher switching rates with increasing laser power. High counts correspond to NV^- state and low counts correspond to NV^0 state

Measuring the ionization rates of the NV center is important for determining a optimal readout of the charge state. As detailed in chapter 2, the ionization rates can be obtained by measuring the autocorrelation function of the fluorescence traces. The autocorrelation was calculated by creating a matrix with each element equal to :

$$T_{i,j} = n(t_i)n(t_j) \tag{5.15}$$

where n(t_i) is the number of counts at time t_i. Averaging over several fluorescence time traces, we get a matrix with exponential decay in the off diagonal (figure 5–5 a). The matrix is further averaged by summing the elements on the diagonal axis which result in a exponential decay such as figure 5–5 b).

Fitting equation 5.13 to figure 5–5 b) allows us to extract values of the ionization rates Γ_- and Γ_+. Values for A_+ and A_- were obtained by histogramming the fluorescence traces. Two clear distributions can be seen from the histogram correponding to the two charge states number of counts. Two poisson distributions are fitted to the histogram and values of A_- and A_+ are extracted from the mean of the Poisson distribution.

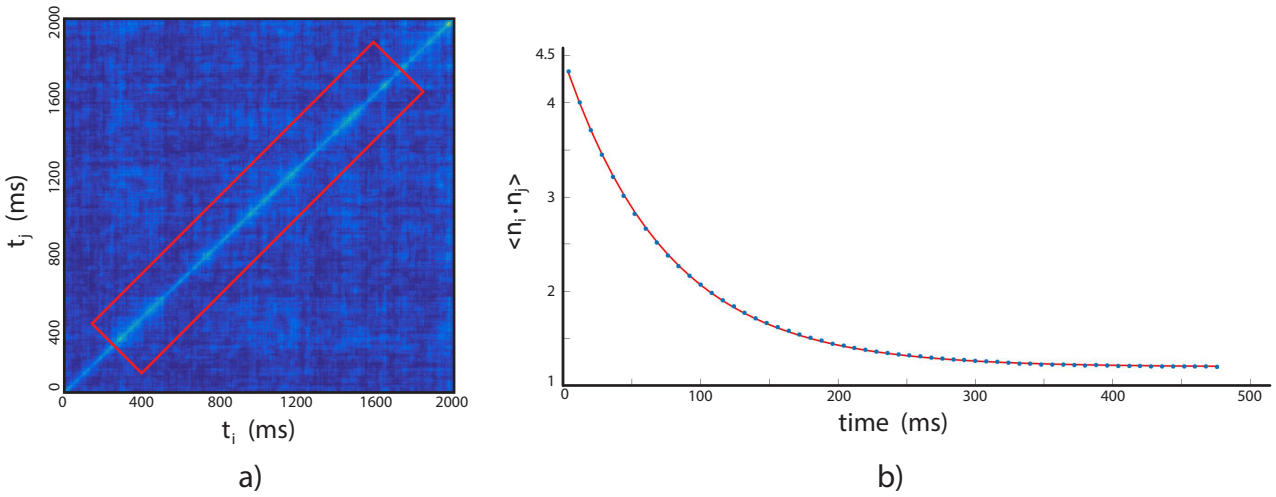

Figure 5–5: a) The covariance matrix $T_{i,j} = n(t_i)n(t_j)$ shows of diagonal decay. b) Averaging over the diagonal axis (red rectangle in a)) reveals an even more precise exponential decay

Rates for both NV centers are shown in figure 5–6 a) and 5–6 b). The error bars were calculated from the difference between traces obtained from solutions of K_0 and Γ or K_1 and Γ. As can be seen rates for NV1 and NV2 are very similar and both are proportional to $\sim I^2$. The rates measured are about 10 times lower than rates measured in other papers [16, 17]. The lower rates measured can be attributed to inefficiencies in coupling yellow excitation to the defects resulting in lower intensity power expected from the measured power going into the objective.

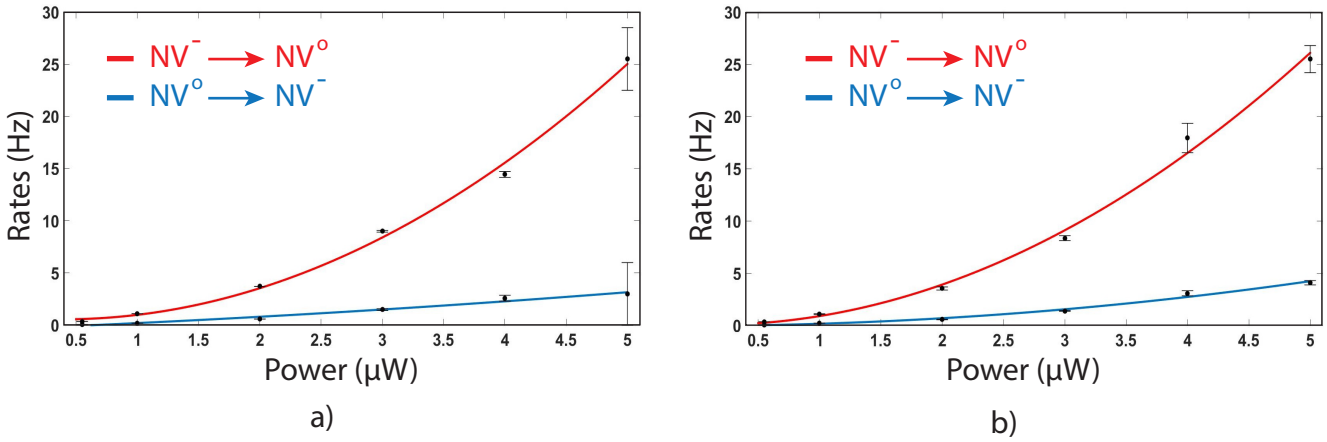

Figure 5–6: Ionization rates measured for NV1 (a) and NV2 (b). The solid line are a least-squares fiiting to the equation aI^2+b, where I is the laser intensity. We see that both NVs have similar ionization rates that are proportional to the square of the laser power.

5.3 Fidelity

Charge state measurement has been used for showing spin to charge conversion in the NV center [17] as well as for subdiffraction optical techniques [19]. Obtaining a fidelity on the charge state measurement is essential and two parameters need to be optimized for finding the best fidelity, the laser power and the time bin (or counting time).

5.3.1 Extracting the Fidelity

Here is a model using poisson distributions to extract the fidelity of charge state measurement. Consider the two Poisson distributions P_1 and P_2 from figure 5–7 which represent the number of counts in the NV^- and NV^o states. The error on the measurement is given by the area under the curve where P1 and P2 interpose. The error ϵ is then given by :

$$\epsilon(\xi) = P(NV^0) \int_{\xi}^{\infty} P(n|NV^o) + P(NV^-) \int_{0}^{\xi} P(n|NV^-) \tag{5.16}$$

where $P(NV^o)$ and $P(NV^-)$ are the normalized Poisson distributions :

$$P(NV^o) = \frac{\int P_1}{\int P_1 + P_2} \quad ; \quad P(NV^-) = \frac{\int P_2}{\int P_1 + P_2} \tag{5.17}$$

and $P(n|NV^o)$ and $P(n|NV^-)$ are the normalized conditional probability of n counts given the state NV^- or NV^- :

$$P(n|NV^-) = \frac{P_1(n)}{\int P_1} \quad ; \quad P(n|NV^o) = \frac{P_2(n)}{\int P_2} \tag{5.18}$$

Finally the fidelity will be given by :

$$F = 1 - \epsilon \tag{5.19}$$

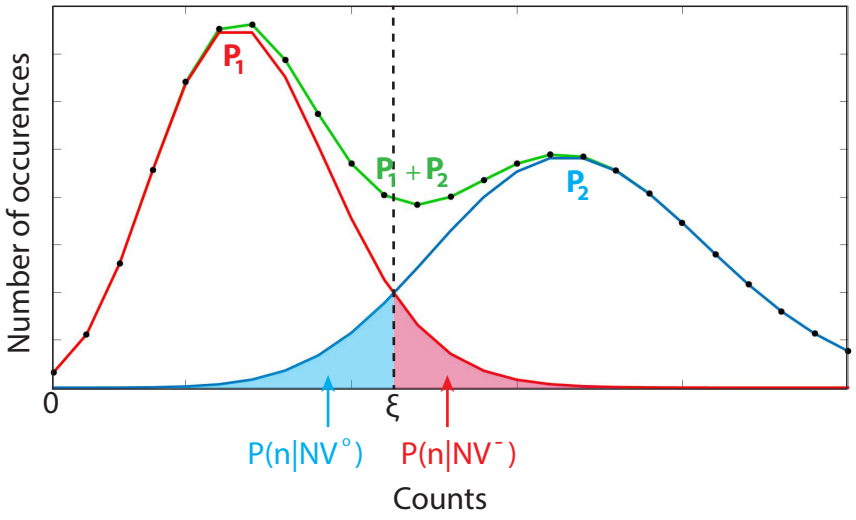

Figure 5–7: Illustration of two Poisson distributions corresponding to NV^- counts (P_1) and NV^o counts (P_2). The error is defined as the sum of the normalized blue and red area

5.3.2 Data

Choosing the value for ξ in equation 5.16 which maximizes the fidelity is important. The value of ξ sets the threshold which separates counts attributed to the charge states NV^- and NV^o. Intuitively, one would think the best value for ξ is at the intersection of both Poisson distributions. Figure 5–8 a) shows the fidelity as a function of ξ for a power of 1 μW and bin size of 4.5 ms. Maximum fidelity is measured for ξ values around 3 to 4 counts, which is equal to the intersection point.

Figure 5–8 b) shows fidelity values for a laser power of 1 μW and 0.55 μW and different bin times. We see that a fidelity of about 97% can be obtained with a power of 1 μW and bin time of 4.5 ms.

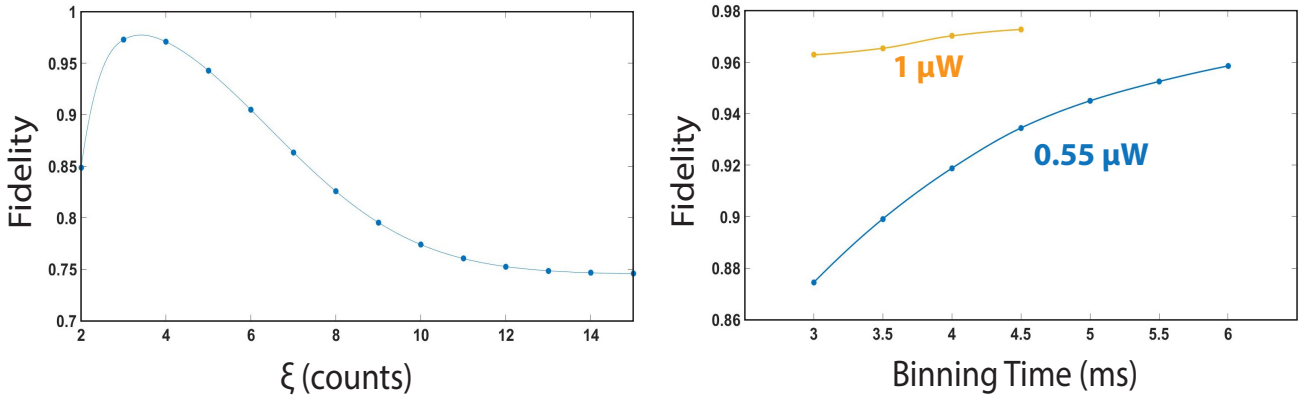

Figure 5–8: a) Fidelity measurement as a function of the threshold number. We see that maximum fidelity is measured for a threshold between 3 and 4 counts which represents the intersection point of the two Poisson distributions. b) Maximum fidelity as a function of bin size and powers of 0.55 μW and 1 μW.

It was not possible to measure fidelity values for powers higher than 1μW due to switching probabilities occurring within the bin time. For example,

figures 5–9 a) and 5–9 b) shows the two Poisson fits for a bin size of 4.5 ms and 7 ms and power of 1 μW. We see that for the 7 ms fit, the sum of the two Poisson distribution is below the total number of counts measured. This is occuring because for higher bin sizes, the probability of switching events is higher which increases the number of counts around the threshold. This increase of counts around the threshold creates an asymmetry in the distribution and a Poisson distribution is not a good fit anymore. However, it is important to note that other groups were able to implement charge state measurement techniques for higher power that use more advanced analysis to incorporate data sets with high probability of switching [17].

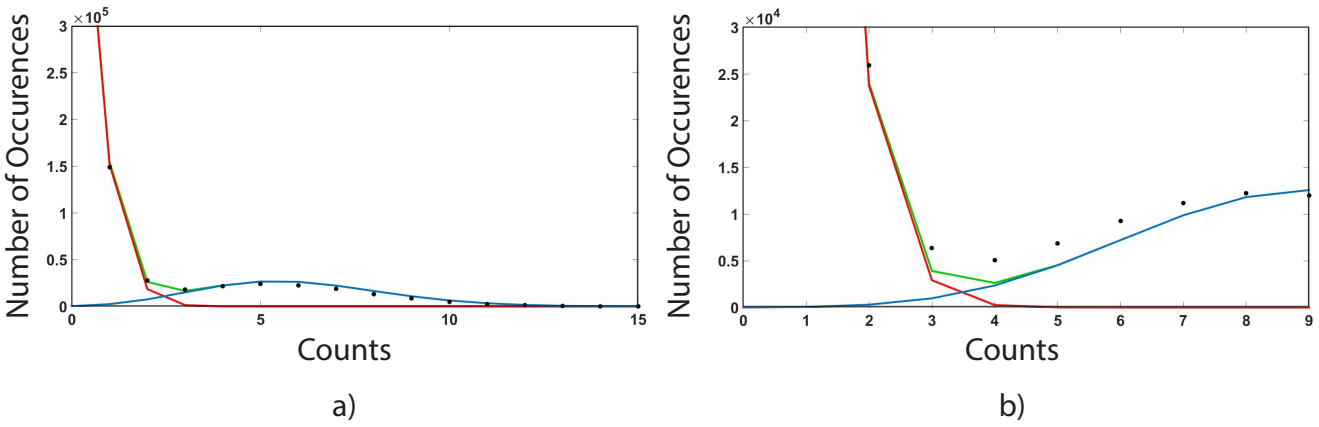

Figure 5–9: a) Histogram of counts for time traces of 1 μW power and 4.5 ms bin size b) Histogram of counts for time traces 1 μW power and 7 ms bin size

CHAPTER 6
Conclusion

In conclusion, the ionization rates of the NV center were measured by calculating the autocorrelation funtion of the fluorescence traces acquired using excitation from a continuous 594 nm laser. A $\sim I^2$ relationship was observed, however the ionization rates measured were about 10 fold lower than rates reported in literature.

The fidelity of the charge state detection of the NV center was calculated and a best value of 97% was measured using a power of 1uW and bin time of 4.5 ms.

For the next steps, one must understand how a single NV center behaves under excitation-depletion cycles and how the cycles affects the electronic charge state ,and the polarization and coherence of the electronic and nuclear spins. Initial experiments, will use Gaussian beams and once the effects on a single NV have been understood, the confocal microscope will be upgraded with STED for studying the measurement capabilities of STED on coupled NV centers.

Appendix A - Spin properties of the NV center

Although not directly related to the subject of this thesis, gaining control over spin degrees of freedom will be important for probing the effect of STED on the polarization and coherence of the electric and nuclear spin state of the NV^-. Since spin manipulation techniques requires the kind of precise timing control that the FPGA program delivers, initial work on room-temperature coherent manipulation of the spin of a single NV^- has already been made. In this appendix we present some theory and experimental techniques regarding spin manipulation of the NV center.

6.1 Spin manipulation

Control of the NV^- center spin state is possible using microwave fields near resonance with the $m_s = 0$ and $m_s = \pm 1$ spin states energy gap. But first let us look at the NV^- spin Hamiltonian in the presence of a magnetic field $\vec{B}$ [37] :

$$H_{NV} = DS_z^2 + g\mu_B \vec{B} \cdot \vec{S} + \sum_{\sigma} \vec{S} \bar{A}_\sigma \vec{I}_\sigma \tag{6.1}$$

$\vec{S}$ is the NV center spin operator, $\bar{A}_\sigma$ is the hyperfine tensor and I_σ is the spin operator of nearby nuclei. The first term DS_z^2 describes the zero-field splitting of the NV center, while the next term $g\mu_B \vec{B} \cdot \vec{S}$ represents the Zeeman-splitting. A constant magnetic field parallel to S_z will split the degeneracy between $m_s = \pm 1$ spin states. An oscillating magnetic field, $B(t) = B_\perp \cos \nu t$, perpendicular to S_z will drive Rabi oscillations (figure 6–1) at frequency :

$$\Omega_R^2 = \Omega^2 + \Delta^2 \tag{6.2}$$

where $\Omega = g\mu_B B_\perp$ is the coupling strength and Δ is the detuning. The final term $\sum_\sigma \vec{S}\bar{A}_\sigma\vec{I}_\sigma$ describes the hyperfine interactions and includes information on how the spin state energies change in the presence of nearby nuclei such as ^{13}C, ^{14}N and ^{15}N.

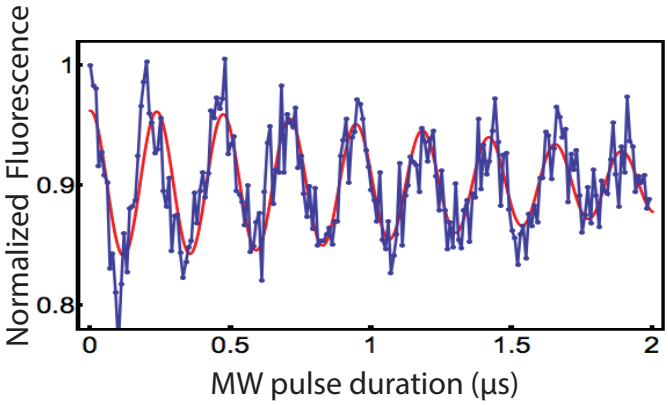

Figure 6–1: Rabi oscillations between the $m_s = 0$ and $m_s = -1$ spin state. A solid magnet under the sample was used to break the degeneracy between the $m_s = \pm 1$ spin states.

Electron spin resonance (ESR) experiments allow you to measure each of the spin transitions within the NV^- ground state. They are performed by sweeping a microwave field frequency (ω) near the resonant frequency (ω_0) of the NV^- spin states, which will drive transitions between the $m_s = 0$ and $m_s = \pm 1$ spin states. The mixing gets stronger as ω is closer to ω_0, resulting in a dip in the NV^- fluorescence. Figure 6–2 a) shows the 2.87 Ghz resonant frequency between the $m_s = 0$ and $m_s = \pm 1$ spin states, 6–2 b) shows the $m_s = \pm 1$ spin state splitting when applying a constant magnetic field and 6–2 c) show the

hyperfine structure from the presence of a nearby ^{14}N with $I = 1$ leading to 3 lines in each electron spin transition.

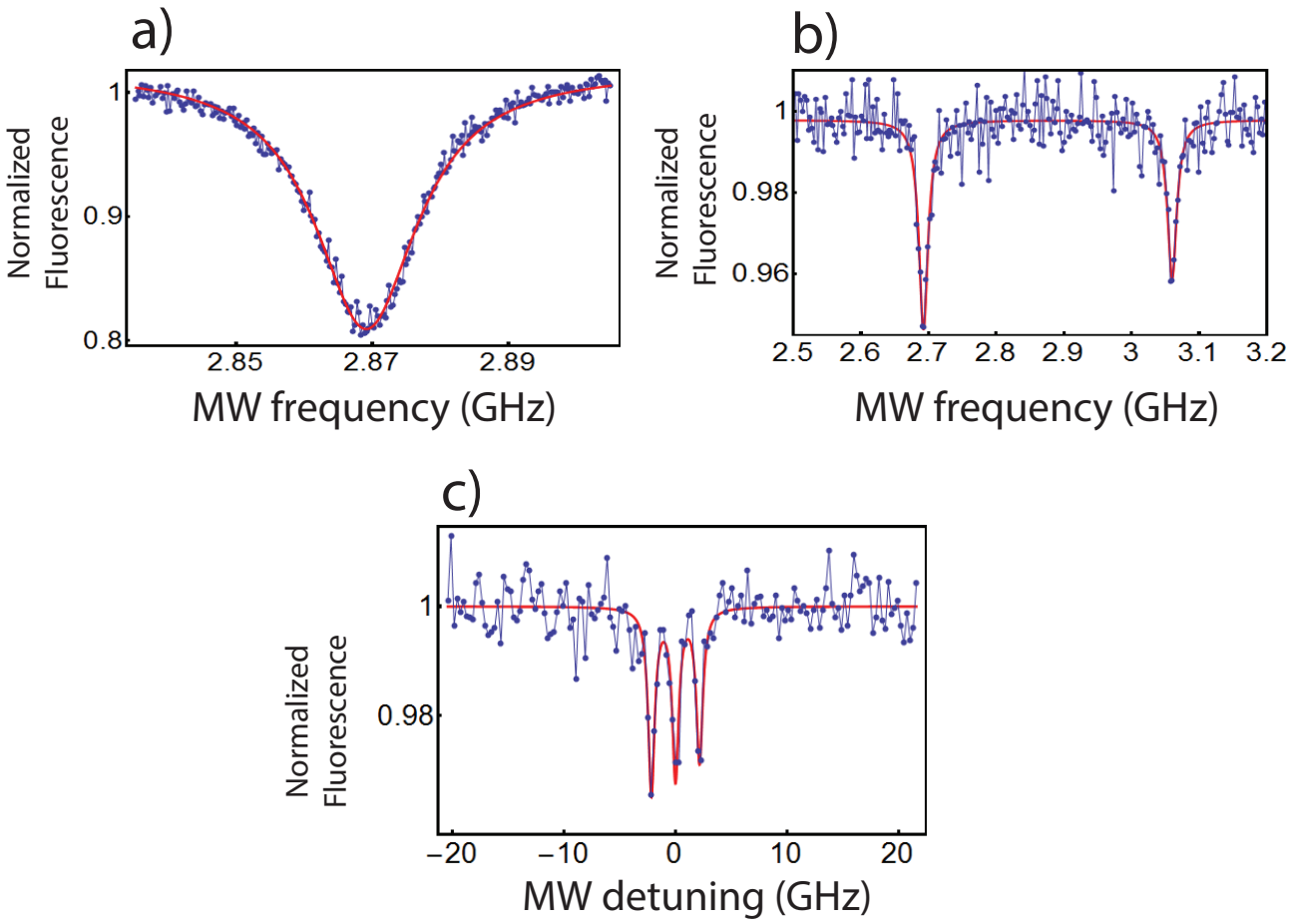

Figure 6–2: a) ESR without an external magnetic field b) ESR with an external field breaks the degeneracy of the $m_s = 0$ and $m_s = \pm 1$ spin state c) ESR reveals hyperfine interaction with a $I = 1$ ^{14}N nucleus

6.2 Pulse protocol for spin manipulation

This section gives further information on how the pulse pattern generator software is used when performing Electron Spin Resonance (ESR) and Rabi

experiments. For ESR experiments the frequency of a MW generator (SMIQ 03B) is varied around the resonance frequency of the NV center. Figure 6–3 illustrates the pulse protocol.

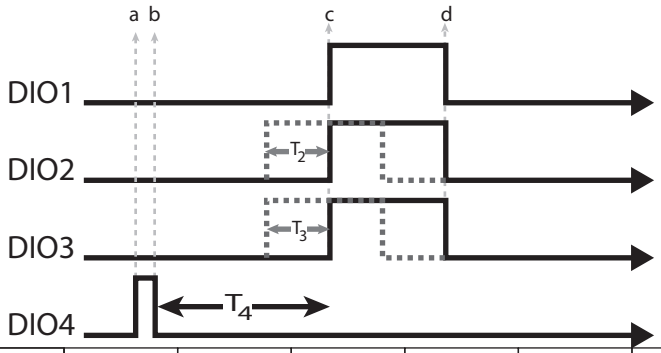

Channel	Delay Start	Delay Stop	Start	Stop	Step Start	Step Stop
1	0	0	c	d	0	0
2	T2	0	c	d	0	0
3	T3	0	c	d	0	0
4	0	0	a	b	0	0

Figure 6–3: DIO1 is used as a software gate and sets the counting time. DIO2 is connected to the laser's AOM and is used to turn On/Off the laser. DIO3 is connected the MW circuit switch and turns On/Off the MW signal. DIO4 is connected to the SMIQ03b in frequency ramping mode. Every TTL pulse adds another increment to the previous MW fequency. The times T_2 and T_3 are delays attributed to the AOM and the switch.

For Rabi experiments the SMIQ03B frequency is set at the resonant frequency of the NV center, but the pulse width is varied. Figure 6–4 illustrates the pulse protocol.

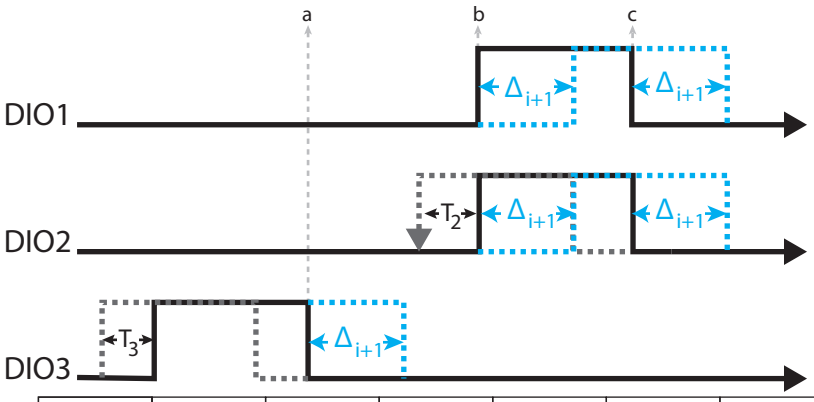

Channel	Delay Start	Delay Stop	Start	Stop	Step Start	Step Stop
1	0	0	b	c	Δ	Δ
2	T2	0	b	c	Δ	Δ
3	T3	0	0	a	0	Δ

Figure 6–4: DIO1 is used as a software gate and sets the counting time. DIO2 is connected to the laser's AOM and is used to turn On/Off the laser. DIO3 is connected the MW circuit switch and turns On/Off the MW signal. The times T_2 and T_3 are delays attributed to the AOM and the switch. The time Δ_{i+1} is added to both the start and stop of DIO1 and DIO2, which effectively translates the counting time. However, Δ_{i+1} is only added to the stop of the DIO3 which increases the MW width pulse.

Appendix B - FPGA dead time

As explained in Chapter 4, due to very a deterministic timed loop, the DIOs can be read or set every clock cycle of the FPGA card, i.e. every 8.3 ns. On the other hand the AOs can only be reset every cycle of the Target VI, which depends on the timing of the pulse sequence and the Host computer timing.

Measuring the dead time Δ_{Host} between the stop of a cycle of the FPGA and the start of another is important for estimating the duty cycle. The biggest factor affecting the FPGA dead time is the amount time required to write the DIOs pulse sequence through the Host to Target DMA. The DIOs pulse sequence is written to the FPGA through a 1D U32 array (see table 4–1). The number of data (N) in this array represents the number of different instructions written in the pulse pattern.

Figure 6–5 shows the measured Δ_{Host} as a function of N. The measurements were obtained by creating a single pulse of 1 μs long, using one DIO channel. A 1 μs pulse is equivalent to N = 4 data written to the Host to Target DMA. Increasing the number of 1 μs pulses increases N. The delay Δ_{Host} was determined using an oscilloscope and measuring the spacing between the first and second train pulse.

We see that for $N < 2 \cdot 10^4$, delays between 1.25 ms and 3.8 ms are measured. For values of $N > 2 \cdot 10^4$ the delay is constant and equal to 3.8 ms. These results can be interpreted by the fact that the Host to Target DMA cannot hold more than $\sim 2 \cdot 10^4$ data, which is ultimately because we don't have much block RAM in the FPGA. For larger values, the Target VI starts and the remaining data is written to the Host to Target DMA when space is available.

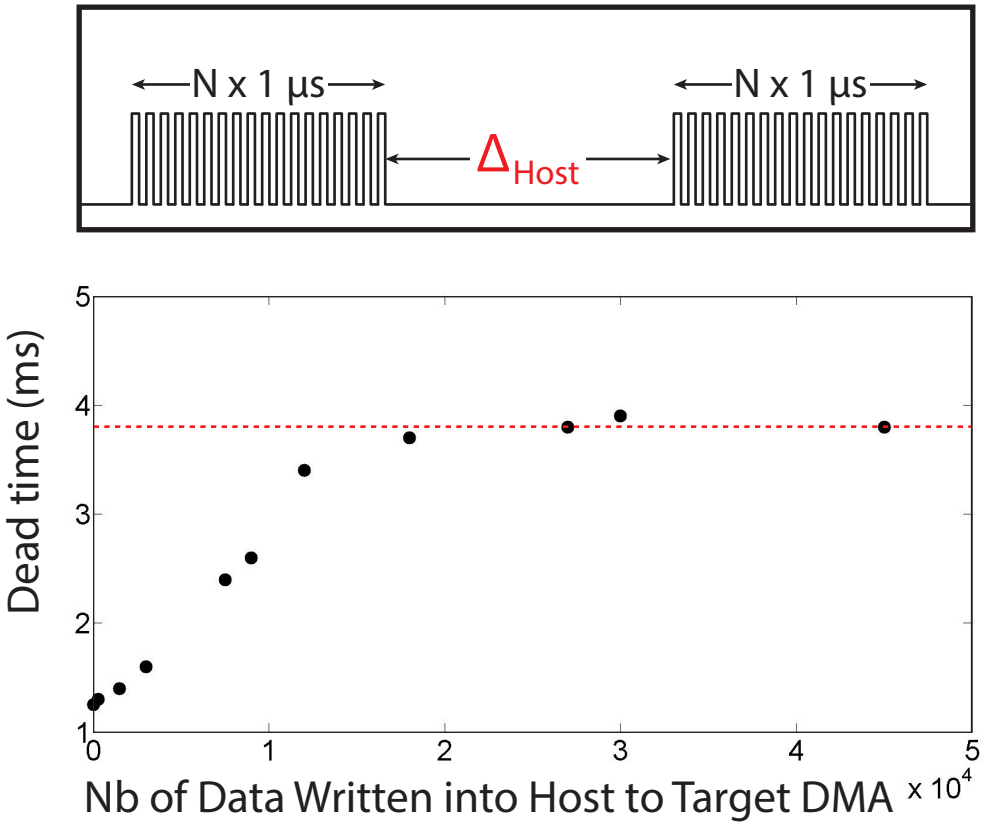

Figure 6–5: The following graph present the delay time between the stop of a cycle of the target VI and the start of another.

REFERENCES

[1] Richard P Feynman. Simulating physics with computers. *International journal of theoretical physics*, 21(6/7):467–488, 1982.

[2] David Deutsch. Quantum theory, the church-turing principle and the universal quantum computer. In *Proceedings of the Royal Society of London A: Mathematical, Physical and Engineering Sciences*, volume 400, pages 97–117. The Royal Society, 1985.

[3] Peter W Shor. Algorithms for quantum computation: Discrete logarithms and factoring. In *Foundations of Computer Science, 1994 Proceedings., 35th Annual Symposium on*, pages 124–134. IEEE, 1994.

[4] Alberto Politi, Jonathan CF Matthews, and Jeremy L O'Brien. Shors quantum factoring algorithm on a photonic chip. *Science*, 325(5945):1221–1221, 2009.

[5] Dietrich Leibfried, Brian DeMarco, Volker Meyer, David Lucas, Murray Barrett, Joe Britton, WM Itano, B Jelenković, Chris Langer, Till Rosenband, et al. Experimental demonstration of a robust, high-fidelity geometric two ion-qubit phase gate. *Nature*, 422(6930):412–415, 2003.

[6] Toshiki Hayashi, Toshimasa Fujisawa, Hai-Du Cheong, Yoon Hee Jeong, and Yoshiro Hirayama. Coherent manipulation of electronic states in a double quantum dot. *Physical review letters*, 91(22):226804, 2003.

[7] John M Martinis, S Nam, J Aumentado, and C Urbina. Rabi oscillations in a large josephson-junction qubit. *Physical Review Letters*, 89(11):117901, 2002.

[8] Jones, J. A. and Mosca, M. Implementation of a quantum algorithm to solve Deutschs problem on a nuclear magnetic resonance quantum computer. J. Chem. Phys. (in the press); also LANL preprint quant-ph/9801027.

[9] JR Petta, Alexander Comstock Johnson, JM Taylor, EA Laird, A Yacoby, Mikhail D Lukin, CM Marcus, MP Hanson, and AC Gossard. Coherent manipulation of coupled electron spins in semiconductor quantum dots. *Science*, 309(5744):2180–2184, 2005.

[10] Wolfgang Harneit. Fullerene-based electron-spin quantum computer. *Physical Review A*, 65(3):032322, 2002.

[11] Marcus W Doherty, Neil B Manson, Paul Delaney, Fedor Jelezko, Jörg Wrachtrup, and Lloyd CL Hollenberg. The nitrogen-vacancy colour centre in diamond. *Physics Reports*, 528(1):1–45, 2013.

[12] MV Gurudev Dutt, L Childress, L Jiang, E Togan, J Maze, F Jelezko, AS Zibrov, PR Hemmer, and MD Lukin. Quantum register based on individual electronic and nuclear spin qubits in diamond. *Science*, 316(5829):1312–1316, 2007.

[13] F Dolde, I Jakobi, B Naydenov, N Zhao, S Pezzagna, C Trautmann, J Meijer, P Neumann, F Jelezko, and J Wrachtrup. Room-temperature entanglement between single defect spins in diamond. *Nature Physics*, 9(3):139–143, 2013.

[14] P Neumann, R Kolesov, B Naydenov, J Beck, F Rempp, M Steiner, V Jacques, G Balasubramanian, ML Markham, DJ Twitchen, et al. Quantum register based on coupled electron spins in a room-temperature solid. *Nature Physics*, 6(4):249–253, 2010.

[15] Dominik Wildanger, Jeronimo R Maze, and Stefan W Hell. Diffraction unlimited all-optical recording of electron spin resonances. *Physical review letters*, 107(1):017601, 2011.

[16] N Aslam, G Waldherr, P Neumann, F Jelezko, and J Wrachtrup. Photo-induced ionization dynamics of the nitrogen vacancy defect in diamond investigated by single-shot charge state detection. *New Journal of Physics*, 15(1):013064, 2013.

[17] BJ Shields, QP Unterreithmeier, NP de Leon, H Park, and MD Lukin. Efficient readout of a single spin state in diamond via spin-to-charge conversion. *Phys. Rev. Lett. 114, 136402*, 31 March 2015.

[18] JR Maze, Adam Gali, Emre Togan, Yiwen Chu, Alexei Trifonov, Efthimios Kaxiras, and MD Lukin. Properties of nitrogen-vacancy centers in diamond: the group theoretic approach. *New Journal of Physics*, 13(2):025025, 2011.

[19] Xiangdong Chen, Changling Zou, Zhaojun Gong, Chunhua Dong, Guangcan Guo, and Fangwen Sun. Subdiffraction optical manipulation of the charge state of nitrogen vacancy center in diamond. *Light: Science & Applications*, 4(1):e230, 2015.

[20] F Jelezko, C Tietz, A Gruber, I Popa, A Nizovtsev, S Kilin, and J Wrachtrup. Spectroscopy of single nv centers in diamond. *Single Molecules*, 2(4):255–260, 2001.

[21] Lucio Robledo, Hannes Bernien, Toeno van der Sar, and Ronald Hanson. Spin dynamics in the optical cycle of single nitrogen-vacancy centres in diamond. *New Journal of Physics*, 13(2):025013, 2011.

[22] Lilian Isabel Childress. *Coherent manipulation of single quantum systems in the solid state*. PhD thesis, Harvard University Cambridge, Massachusetts, 2007.

[23] Eva Rittweger, Kyu Young Han, Scott E Irvine, Christian Eggeling, and Stefan W Hell. Sted microscopy reveals crystal colour centres with nanometric resolution. *Nature Photonics*, 3(3):144–147, 2009.

[24] Silvia Arroyo-Camejo, Marie-Pierre Adam, Mondher Besbes, Jean-Paul Hugonin, Vincent Jacques, Jean-Jacques Greffet, Jean-François Roch, Stefan W Hell, and François Treussart. Stimulated emission depletion microscopy resolves individual nitrogen vacancy centers in diamond nanocrystals. *ACS nano*, 7(12):10912–10919, 2013.

[25] Dominik Wildanger, Brian R Patton, Heiko Schill, Luca Marseglia, JP Hadden, Sebastian Knauer, Andreas Schönle, John G Rarity, Jeremy L O'Brien, Stefan W Hell, et al. Solid immersion facilitates fluorescence microscopy with nanometer resolution and sub-ångström emitter localization. *Advanced Materials*, 24(44):OP309–OP313, 2012.

[26] NB Manson and JP Harrison. Photo-ionization of the nitrogen-vacancy center in diamond. *Diamond and related materials*, 14(10):1705–1710, 2005.

[27] Katja Beha, Anton Batalov, Neil B Manson, Rudolf Bratschitsch, and Alfred Leitenstorfer. Optimum photoluminescence excitation and recharging cycle of single nitrogen-vacancy centers in ultrapure diamond. *Physical review letters*, 109(9):097404, 2012.

[28] P Siyushev, H Pinto, M Vörös, A Gali, F Jelezko, and J Wrachtrup. Optically controlled switching of the charge state of a single nitrogen-vacancy center in diamond at cryogenic temperatures. *Physical review letters*, 110(16):167402, 2013.

[29] Stephen W Paddock. Principles and practices of laser scanning confocal microscopy. *Molecular biotechnology*, 16(2):127–149, 2000.

[30] Paschotta, Dr. 'Encyclopedia Of Laser Physics And Technology - Acousto-Optic Modulators, AOM, Bragg Cells'. Rp-photonics.com. N.p., 2015. Web. 30 Apr. 2015.

[31] Paschotta, Dr. 'Encyclopedia Of Laser Physics And Technology - Mode Cleaners, Spatial Filter, Mode Cleaner Cavities, Beam Quality'. Rp-photonics.com. N.p., 2015. Web. 30 Apr. 2015.

[32] Microscopyu.com,. 'Nikon Microscopyu — Introduction To Microscope Objectives'. N.p., 2015. Web. 30 Apr. 2015.

[33] Dingwei Zheng. *Study and manipulation of photoluminescent NV color center in diamond*. PhD thesis, École normale supérieure de Cachan-ENS Cachan; East China Normal University, 2010.

[34] F Ziegler, D Beck, H Brand, H Hahn, G Marx, and L Schweikhard. A new pulse-pattern generator based on labview fpga. *Nuclear Instruments and Methods in Physics Research Section A: Accelerators, Spectrometers, Detectors and Associated Equipment*, 679:1–6, 2012.

[35] Xilinx.com,. 'What Is A FPGA?'. N.p., 2015. Web. 30 Apr. 2015.

[36] Alexios Beveratos, Rosa Brouri, J-P Poizat, and Philippe Grangier. Bunching and antibunching from single nv color centers in diamond. In *Quantum Communication, Computing, and Measurement 3*, pages 261–267. Springer, 2002.

[37] R Hanson, O Gywat, and DD Awschalom. Room-temperature manipulation and decoherence of a single spin in diamond. *Physical Review B*, 74(16):161203, 2006.